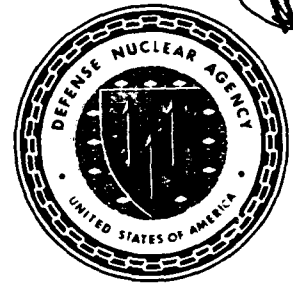




Defense Nuclear Agency
Alexandria, VA 22310-3398



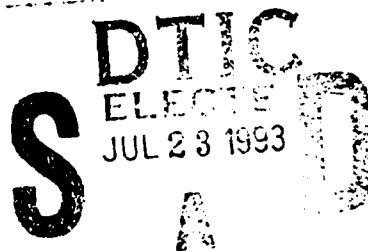
AD-A267 069



DNA-TR-92-153

Determination of the Electromagnetic Fields Radiated from the ARES EMP Simulator

Fred M. Tesche
Charles T. C. Mo
Logicon RDA
P.O. Box 92500
Los Angeles, CA 90009



July 1993

Technical Report

CONTRACT No. DNA 001-88-C-0046

Approved for public release;
distribution is unlimited.

93-16650



424215

Destroy this report when it is no longer needed. Do not return to sender.

PLEASE NOTIFY THE DEFENSE NUCLEAR AGENCY,
ATTN: CSTI, 6801 TELEGRAPH ROAD, ALEXANDRIA, VA
22310-3398, IF YOUR ADDRESS IS INCORRECT, IF YOU
WISH IT DELETED FROM THE DISTRIBUTION LIST, OR
IF THE ADDRESSEE IS NO LONGER EMPLOYED BY YOUR
ORGANIZATION.



DISTRIBUTION LIST UPDATE

This mailer is provided to enable DNA to maintain current distribution lists for reports. (We would appreciate your providing the requested information.)

- ☐ Add the individual listed to your distribution list.
- ☐ Delete the cited organization/individual.
- ☐ Change of address.

NOTE:

Please return the mailing label from the document so that any additions, changes, corrections or deletions can be made easily.

NAME: _____

ORGANIZATION: _____

OLD ADDRESS**CURRENT ADDRESS**

TELEPHONE NUMBER: () _____

DNA PUBLICATION NUMBER/TITLE**CHANGES/DELETIONS/ADDITIONS, etc.)**
(Attach Sheet if more Space is Required)

DNA OR OTHER GOVERNMENT CONTRACT NUMBER: _____

CERTIFICATION OF NEED-TO-KNOW BY GOVERNMENT SPONSOR (if other than DNA): _____

SPONSORING ORGANIZATION: _____

CONTRACTING OFFICER OR REPRESENTATIVE: _____

SIGNATURE: _____

CUT HERE AND RETURN



DEFENSE NUCLEAR AGENCY
ATTN: TITL
6801 TELEGRAPH ROAD
ALEXANDRIA, VA 22310-3398

DEFENSE NUCLEAR AGENCY
ATTN: TITL
6801 TELEGRAPH ROAD
ALEXANDRIA, VA 22310-3398

REPORT DOCUMENTATION PAGE			Form Approved OMB No. 0704-0188	
Public reporting burden for this collection of information is estimated to average 1 hour per response including the time for reviewing instructions, searching existing data sources, gathering and maintaining the data needed, and completing and reviewing the collection of information. Send comments regarding this burden estimate or any other aspect of this collection of information, including suggestions for reducing this burden, to Washington Headquarters Services, Directorate for Information Operations and Reports, 1215 Jefferson Davis Highway, Suite 1204, Arlington, VA 22202-4302, and to the Office of Management and Budget, Paperwork Reduction Project (0704-0188), Washington, DC 20503				
1. AGENCY USE ONLY (Leave blank)	2. REPORT DATE 930701	3. REPORT TYPE AND DATES COVERED Technical 910901 - 921231		
4. TITLE AND SUBTITLE Determination of the Electromagnetic Fields Radiated from the ARES EMP Simulator		5. FUNDING NUMBERS C - DNA 001-88-C-0046 PE - 62715H PR - RD TA - RC WU - DH105015		
6. AUTHOR(S) Fred M. Tesche and Charles T. C. Mo				
7. PERFORMING ORGANIZATION NAME(S) AND ADDRESS(ES) Logicon RDA P.O. Box 92500 Los Angeles, CA 90009		8. PERFORMING ORGANIZATION REPORT NUMBER TR-2-2240-1704-0001		
9. SPONSORING/MONITORING AGENCY NAME(S) AND ADDRESS(ES) Defense Nuclear Agency 6801 Telegraph Road Alexandria, VA 22310-3398 FCTT/Shoup		10. SPONSORING/MONITORING AGENCY REPORT NUMBER DNA-TR-92-153		
11. SUPPLEMENTARY NOTES This work was sponsored by the Defense Nuclear Agency under RDT&E RMC Codes B4662D RD RC 00021 DFPR 1910A 25904D and B4662D RD RC 00016 DFPR 1910A 25904D.				
12a. DISTRIBUTION/AVAILABILITY STATEMENT Approved for public release; distribution is unlimited.			12b. DISTRIBUTION CODE	
13. ABSTRACT (Maximum 200 words) This report describes a calculational model for evaluating the electromagnetic (EM) fields produced by the ARES simulator outside its normal working volume. The model employs transmission line theory to determine the simulator current distribution. Once this is determined, the radiated fields are computed approximately using the Norton surface-wave formalism. The transient electric and magnetic fields on the ground are calculated using a fast Fourier transform (FFT) and are compared with experimental magnetic field data. Accuracies on the order of 30% in the peak fields are noted in much of the data. The fields in the air above the earth also have been calculated, and the relative importance of the Norton surface wave in the overall solution has been clarified. This model and its resulting PC code provide a useful tool for further studies of the impact of radiated EM fields on distant electrical systems. The results presented here are directly applicable in defining and evaluating the EM environments produced by ARES, or by similar bounded wave simulators, and in assessing and limiting the possible biological effects of pulsed radiation.				
14. SUBJECT TERMS EMP Fields EMP Simulator			15. NUMBER OF PAGES 66	
			16. PRICE CODE	
17. SECURITY CLASSIFICATION OF REPORT UNCLASSIFIED	18. SECURITY CLASSIFICATION OF THIS PAGE UNCLASSIFIED	19. SECURITY CLASSIFICATION OF ABSTRACT UNCLASSIFIED	20. LIMITATION OF ABSTRACT SAR	

UNCLASSIFIED

SECURITY CLASSIFICATION OF THIS PAGE

CLASSIFIED BY:

N/A since Unclassified.

DECLASSIFY ON:

N/A since Unclassified.

SECURITY CLASSIFICATION OF THIS PAGE

UNCLASSIFIED

PREFACE

This work has been sponsored by the Defense Nuclear Agency (DNA), under Contract DNA001-88-C-0046 with Logicon/RDA. The authors acknowledge the helpful technical discussions and support of the following people during the course of these investigations:

- Dr. George Baker, Col. Berry Hansen, Headquarters, DNA
- Capt. Bill Cowan, Mr. Bill Summa, Field Command, DNA
- Dr. Carl Baum, Phillips Laboratory
- Dr. Kelvin Lee, Kaman/Dikewood
- Dr. J. Philip Castillo, Logicon/RDA

Accession For	
NTIS CRA&I	<input checked="checked" type="checkbox"/>
DTIC TAB	<input type="checkbox"/>
Unannounced	<input type="checkbox"/>
Justification	
By	
Distribution/	
Availability Codes	
Dist	Avail and/or Special
A-1	

CONVERSION TABLE

Conversion factors for U.S. Customary to metric (SI) units of measurement.

MULTIPLY \longrightarrow BY \longrightarrow TO GET
TO GET \longleftarrow BY \longleftarrow DIVIDE

angstrom	1.000 000 X E -10	meters (m)
atmosphere (normal)	1.013 25 X E +2	kilo pascal (kPa)
bar	1.000 000 X E +2	kilo pascal (kPa)
barn	1.000 000 X E -28	meter ² (m ²)
British thermal unit (thermochemical)	1.054 350 X E +3	joule (J)
calorie (thermochemical)	4.184 000	joule (J)
cal (thermochemical)/cm ²	4.184 000 X E -2	mega joule/m ² (MJ/m ²)
curie	3.700 000 X E +1	giga becquerel (GBq)*
degree (angle)	1.745 329 X E -2	radian (rad)
degree Fahrenheit	$T = (t^{\circ}F + 459.67)/1.8$	degree kelvin (K)
electron volt	1.602 19 X E -19	joule (J)
erg	1.000 000 X E -7	joule (J)
erg/second	1.000 000 X E -7	watt (W)
foot	3.048 000 X E -1	meter (m)
foot-pound-force	1.355 818	joule (J)
gallon (U.S. liquid)	3.785 412 X E -3	meter ³ (m ³)
inch	2.540 000 X E -2	meter (m)
jerk	1.000 000 X E +9	joule (J)
joule/kilogram (J/kg) (radiation dose absorbed)	1.000 000	Gray (Gy)**
kilotons	4.183	terajoules
kip (1000 lbf)	4.448 222 X E +3	newton (N)
kip/inch ² (ksi)	6.894 757 X E +3	kilo pascal (kPa)
ktap	1.000 000 X E +2	newton-second/m ² (N-s/m ²)
micron	1.000 000 X E -6	meter (m)
mil	2.540 000 X E -5	meter (m)
mile (international)	1.609 344 X E +3	meter (m)
ounce	2.834 952 X E -2	kilogram (kg)
pound-force (lbf avoirdupois)	4.448 222	newton (N)
pound-force inch	1.129 848 X E -1	newton-meter (N-m)
pound-force/foot	1.751 268 X E +2	newton/meter (N/m)
pound-force/foot ²	4.788 026 X E -2	kilo pascal (kPa)
pound-force/inch ² (psi)	6.894 757	kilo pascal (kPa)
pound-mass (lbm avoirdupois)	4.535 924 X E -1	kilogram (kg)
pound-mass-foot ² (moment of inertia)	4.214 011 X E -2	kilogram-meter ² (kg-m ²)
pound-mass/foot ³	1.601 846 X E +1	kilogram/meter ³ (kg/m ³)
rad (radiation dose absorbed)	1.000 000 X E -2	Gray (Gy)**
roentgen	2.579 760 X E -4	coulomb/kilogram (C/kg)
shake	1.000 000 X E -8	second (s)
slug	1.459 390 X E +1	kilogram (kg)
torr (mm Hg, 0°C)	1.333 22 X E -1	kilo pascal (kPa)

* The becquerel (Bq) is the SI unit of radioactivity; 1 Bq = 1 event/s.

**The Gray (Gy) is the SI unit of absorbed radiation.

TABLE OF CONTENTS

Section	Page
PREFACE	iii
CONVERSION TABLE	iv
FIGURES	vi
1 INTRODUCTION	1
2 THE CALCULATIONAL MODEL	3
2.1 ARES PHYSICAL CONFIGURATION.	3
2.2 ARES ELECTRICAL MODEL.	5
2.3 THE ANALYSIS PROCEDURE	5
2.3.1 General Considerations.	5
2.3.2 Transmission Line Model For The Simulator Current.	7
2.3.3 Evaluation of The Radiated Fields.	8
3 MODEL VALIDATION	18
3.1 FIELD MEASUREMENTS ON THE GROUND.	18
3.2 FIELD MEASUREMENTS IN THE AIR.	23
3.3 INVESTIGATION OF WAVEFORM CHARACTERISTICS.	24
4 NUMERICAL RESULTS	27
4.1 TRANSIENT FIELDS ON THE GROUND.	27
4.2 DEPENDENCE OF GROUND FIELDS ON RANGE.	27
4.3 IMPORTANCE OF THE SURFACE WAVE.	31
4.4 TRANSIENT E-FIELDS ABOVE THE GROUND.	31
4.5 SPATIAL PATTERN OF PEAK FIELDS IN THE AIR.	34
4.6 E AND H-FIELDS NEAR THE SIMULATOR.	38
5 ESTIMATES OF TERRAIN EFFECTS	40
6 ARES PULSER RISE TIME EFFECTS	44
7 COMPUTER CODE DESCRIPTION	48
7.1 CODE OVERVIEW.	48
7.2 COMPUTER REQUIREMENTS FOR ANALYSIS.	50
8 SUMMARY	51
REFERENCES	52
Appendix	
ACRONYMS	54

FIGURES

Figure	Page
2-1 The ARES simulator.	3
2-2 The vertical E-field environment within the ARES working volume, measured at 78 meters from the pulser.	4
2-3 ARES electrical model and co-ordinate system.	6
2-4 Transmission line model for the simulator current.	7
2-5 Discrete Simulator current elements producing a radiated field.	9
2-6 Field components produced by an infinitesimal current element over the earth.	10
2-7 Geometry for a vertical current element.	10
2-8 Geometry for a horizontal current element.	13
2-9 Simplification of the integration process for distant, airborne observation points.	15
2-10 Geometry for calculating the radiated fields from a wire segment of length L	16
3-1 Radiated fields on the ground away from ARES.	18
3-2 Measured H-field at location #17, from [8].	19
3-3 Calculated principal H- and E-field components at point # 17.	20
3-4 Contours of total peak H-field in A/m on the ground (experimental points from [8] are marked by Δ).	21
3-5 Contours of total peak E-field in V/m on the ground.	22
3-6 Plot of the calculated total transient H-field magnitude at $(x,y,z) = (-1025, -1617, 61)$ m.	23
3-7 Radiated E_z field at $(x,y,z) = (10,10,10)$ km.	24
3-8 ARES impulse excitation (a) and radiated E_z field responses (b) and (c) at $(x,y,z) = (10, 10, 10)$ km.	25
3-9 Waveform contributions at point O.	26

FIGURES (Continued)

Figure	Page
4-1 Plots of the transient H-field components on the ground to the North of ARES.....	28
4-2 Plots of the transient E-field components on the ground to the North of ARES.....	29
4-3 Variations of peak transient fields with range.....	30
4-4 Plots of the peak transient H- and E-fields for different heights at $(x,y) = (2, 2)$ km.....	32
4-5 Far-field E_θ component of ARES for an airborne observer at $r = 20$ km and different values of the angle, θ	33
4-6 Contours of peak H-field (in A/m) for different altitudes.....	35
4-7 Contours of peak E-field (in V/m) for different altitudes.....	36
4-8 Spatial Peak of distant E- and H-field patterns.....	37
4-9 Contours of peak H-field (A/m) on the ground near the simulator.....	38
4-10 Contours of peak E-field (V/m) on the ground near the simulator.....	39
5-1 Ground topography near ARES.....	41
5-2 Digitized ground topography.....	42
5-3 Ground elevation along the straight-line path in Figure 5-2.....	43
5-4 Additional surface wave path-length.....	43
6-1 ARES excitation waveform for various N.....	45
6-2 E_z -field in the air at $(x,y,z) = (0.1, 20, 10)$ km for various N.....	46
6-3 E_z -field on the ground at $(x,y,z) = (0.1, 2, 0)$ km for various N.....	47
7-1 Summary of the ARES calculational procedure.....	49
7-2 Computer time requirements for analysis.....	50

SECTION 1

INTRODUCTION

Recent concerns about the possible environmental and biological effects of radiated electromagnetic (EM) fields have lead to an increased desire to predict and control such fields at locations away from their source. For system-level electromagnetic pulse (EMP) testing, large-scale bounded-wave simulators have been constructed for the purpose of illuminating operational systems with a fast-rising, large-amplitude transient EM field. Although the behavior of the electric fields (E-fields) and the magnetic fields (H-fields) in the working volume of most EMP simulators is well understood and documented, little attention has been paid to the fields outside the simulator at distances of up to several tens of kilometers. The behavior of the fields at these distances depends not only on the details of the simulator structure and its pulser source, but also on the nature of the lossy ground terrain over which the fields propagate.

An example of such a concern is the effort by the Defense Nuclear Agency (DNA) to measure the behavior of the E- and H-field environments produced by the Advanced Research EMP Simulator (ARES). This simulator, owned and operated by DNA, is a type of bounded-wave simulator that maintains most of its EM field environment within the working volume. Some fields, however, are able to radiate away from the simulator, and it is important to characterize them.

This report discusses a calculational model for predicting these fields, and estimates EM such fields on the ground and in the air at different locations away from the simulator. Section 2 evaluates the EM fields radiated from the simulator by first determining the current flowing on the simulator plates. This is done by approximating the parallel-plate ARES simulator as a two-conductor line using TEM transmission line theory. Then, the expressions developed by Norton for the fields produced by infinitesimal vertical and horizontal current elements over the lossy earth are used as a Green's function to determine the E- and H-fields at field points by integrating over the simulator currents. As this formulation is in the frequency domain, a numerical fast Fourier transform (FFT) is used to obtain the transient field responses.

Since this model invokes approximations, an important aspect of this analysis is to validate its accuracy. This is discussed in Section 3. A previous experimental program has lead to a limited field-mapping of transient H-fields on the earth's surface. Both waveforms and peak transient fields are available for measurement points at distances on the order of

several kilometers away from ARES. The calculated fields agree favorably with these measurements on the ground. A measurement of the H-fields at one point in the air above the simulator has also been made, with quite good agreement with the calculated results. Additional measurements are currently being planned.

This model is then used in Section 4 to predict and assess the behavior of the radiated E- and H-fields of the simulator at different observation locations on the ground and in the air. It is found that as the ground observation location moves away from the simulator, the peak transient fields tend to fall off faster than $1/r$, principally due to the attenuation of the Norton surface wave.

A potentially important issue is determining the effect that the irregular terrain around ARES might have on the radiated fields. A preliminary investigation into this effect is discussed in Section 5. Furthermore, this model can be used to address the effects of changing the ARES pulser rise time on the radiated field. This is discussed in Section 6. Section 7 provides a brief description of the computer software developed for this model, and the report concludes with a summary in Section 8.

SECTION 2

THE CALCULATIONAL MODEL

2.1 ARES PHYSICAL CONFIGURATION.

ARES is a bounded-wave, transmission line simulator [1,2] located over a lossy ground. As shown in Figure 2-1, it consists of a source (pulser) and a terminating load connected together by a top and bottom plate constructed of wire. The plates are in the form of three distinct parts: an input conic section, a parallel plate section, and an output conic section. The geometry and dimensions of these sections are chosen so that the transverse electromagnetic (TEM) wave impedance of the 3-section, 2-conductor system is approximately constant, having a value $Z_c \approx 125 \Omega$.

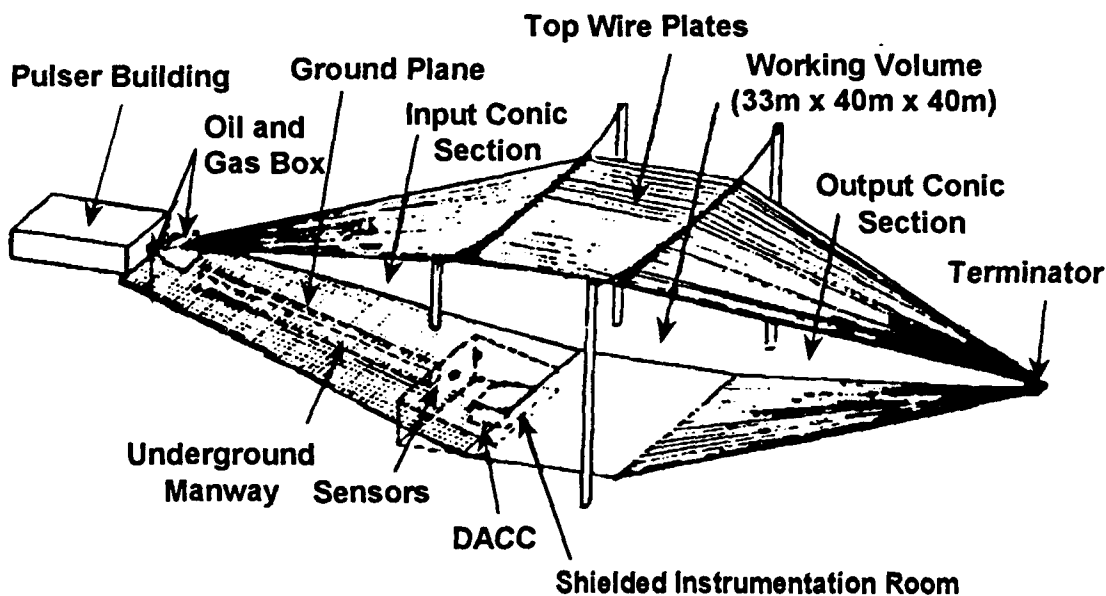
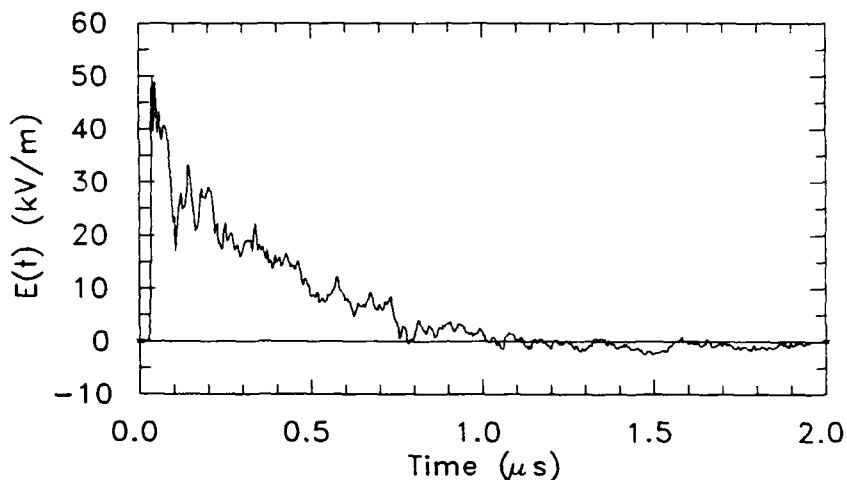


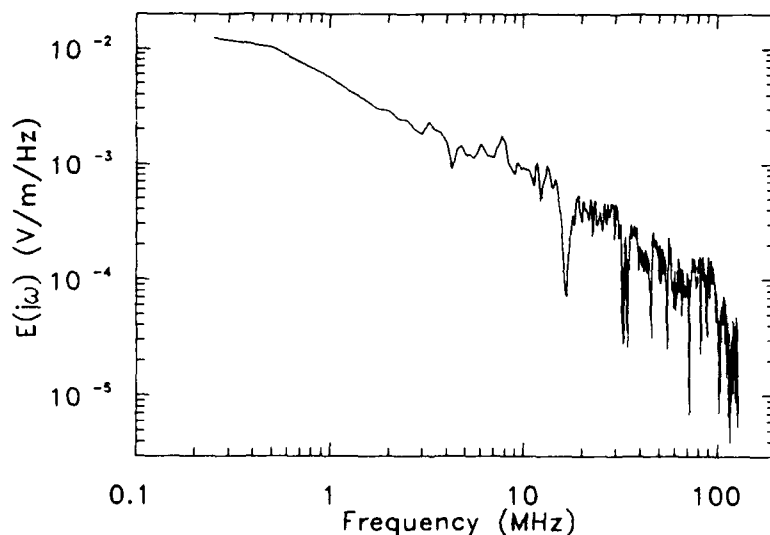
Figure 2-1. The ARES simulator.

The pulser source launches an EM wave into the input conic section and it passes through the parallel plate "working volume" section. Since the terminating load is matched to this characteristic impedance to avoid reflections from the end of the simulator, the wave is mostly absorbed at the end of the output section. Test objects located within the working

volume are exposed to a transient E-field with a peak of about 50 kV/m. Figure 2-2a illustrates a typical time domain waveform within the ARES working volume at a location of 78 meters from the pulser. The zero-to-peak rise time of this field is slightly under 10 ns. Figure 2-2b shows the corresponding frequency spectrum for this environment, and illustrates that frequencies from near dc to over 100 MHz are present in the waveform. This wide band nature of the excitation field requires that the model for predicting the radiated fields from this simulator must also be wide-band.



(a) Transient E-field



(b) Frequency domain spectrum

Figure 2-2. The vertical E-field environment within the ARES working volume, measured at 78 meters from the pulser.

The behavior of the ARES working volume fields is well-known, with detailed mathematical models available [3,4,5]. These fields have also been mapped experimentally [6]. However, only a limited amount of information is available about the fields outside the simulator. An order-of-magnitude estimate of these fields has been reported [7] and some measurements of H-fields on the ground at distant locations have been described [8].

2.2 ARES ELECTRICAL MODEL.

To develop a model for calculating the radiated fields, certain idealizations of the simulator structure are required. As shown in Figure 2-3, the terrain around the simulator is modeled as a flat imperfectly conducting half-space with a conductivity σ_g . Both the pulser and the termination are assumed to be spatial points without geometrical structure, and the electrical conductivity of the parallel plates of the simulator is neglected.

The coordinate system used for this study is shown in Figure 2-3a. The x-axis is along the long direction of the simulator and the z-axis is vertical. The origin of the coordinate system is located on the ground, 20 m directly below the pulser. The location of an arbitrary point and a vector field at this point can be described either by Cartesian (x,y,z) coordinates, spherical coordinates (r, θ, ϕ) , or cylindrical coordinates (ρ, ϕ, z) . These coordinate systems are used interchangeably throughout this report.

Because the field observation locations are assumed to be at distances much greater than the simulator transverse dimensions, a further simplification of the structure can be made. This is shown in Figure 2-3b. For the purpose of computing the radiated fields, the simulator plates are replaced by thin-wire segments. This approximation requires that the field points not be closer than several simulator dimensions in order for the calculated fields to be accurate.

2.3 THE ANALYSIS PROCEDURE.

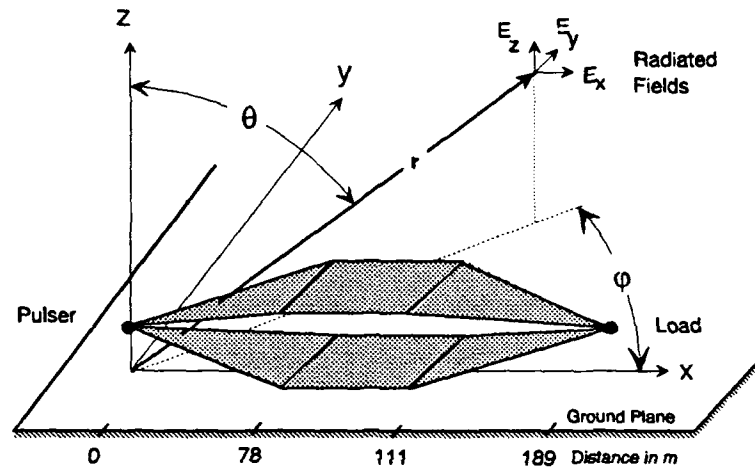
2.3.1 General Considerations.

As shown in Figure 2-3b, the simulator is modeled as a lossless transmission line with separate sections for the wave launcher, the working volume and the termination section. Each section has the same characteristic impedance, but the radiation characteristics are different for each, due to different directions of current flow.

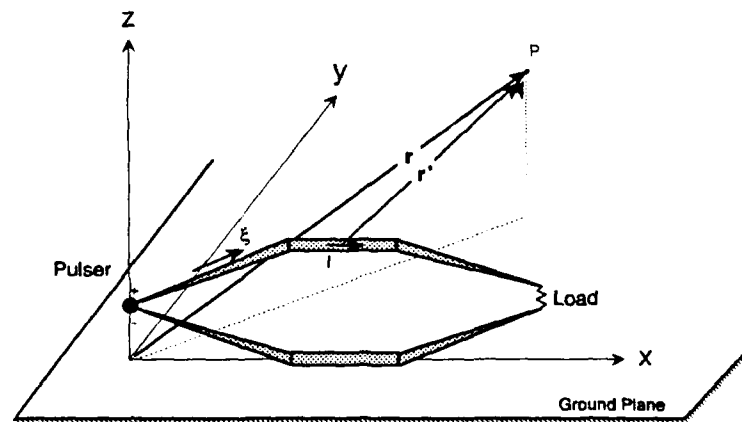
In the frequency domain, the E-field produced at a field point \vec{r} is expressed as an integral over the simulator current distribution using a Green's dyadic function [9,10] as

$$\vec{E}(\vec{r}) = \iint_{\text{Simulator}} \vec{\vec{\Gamma}}(\vec{r}; \vec{r}') \cdot \vec{J}_s(\vec{r}') d\vec{r}' \quad (2.1)$$

Here $\vec{J}_s(\vec{r}')$ is the surface current distribution flowing on the ARES plates, and $\vec{\vec{\Gamma}}(\vec{r}; \vec{r}')$ is the Green's dyadic for the electric field. This dyadic function may be thought of as a 3 by 3 matrix of the E-field components arising from three orthogonal point current elements radiating in the presence of the lossy earth.



(a) Simplified ARES geometry



(b) Wire model of ARES

Figure 2-3. ARES electrical model and coordinate system.

The simplification of the simulator structure shown in Figure 2-3b reduces the two dimensional surface integration of Equation 2.1 to a line integral over the wire segments comprising the simulator. This improves the calculational efficiency of the model, but the validity of this approximation breaks-down as the observation location becomes too close to the simulator. With the coordinate ξ representing the distance along the wire segment in Figure 3b and $\hat{\xi}$ the unit vector in the direction of the wire, the radiated E-field is calculated by

$$\vec{E}(\vec{r}) = \int_{\text{Conductors}} \vec{\Gamma}(\vec{r}; \xi) \cdot \hat{\xi} I(\xi) d\xi \quad (2.2)$$

The task of evaluating the radiated field, therefore, is to evaluate Equation 2.2. To do this, the current on the simulator $I(\xi)$ must be determined, the Green's function $\vec{\Gamma}(\vec{r}; \vec{r}')$ defined, and the indicated integration performed. This analysis is performed in the frequency domain, with transient results being computed using the FFT [11].

2.3.2 Transmission Line Model For The Simulator Current.

The current distribution on the simulator can be determined using a lossless transmission line model shown in Figure 2-4. Because the characteristic impedances of the three simulator sections are equal, a single line with a total length $L = 194$ m is sufficient to describe the behavior of this current. The characteristic impedance of the line is $Z_c \approx 125 \Omega$, and the propagation constant is $\gamma = jk = j\omega/c$, where c is the speed of light in free space. This model neglects the presence of the earth in the determination of the simulator current. That this is a valid approximation may be seen from the fact that most of the simulator current and charge is on the plates, well away from the earth and its influence.

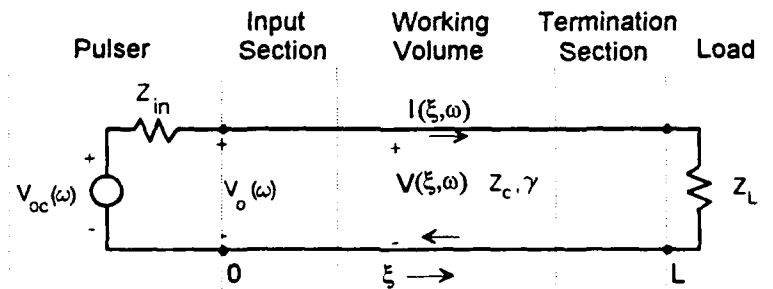


Figure 2-4. Transmission line model for the simulator current.

For the matched line, $Z_L = Z_c$, and the line voltage and current at an arbitrary point ξ along the line are expressed simply as forward propagating traveling waves [12,13] as

$$V(\xi, \omega) = V_o(\omega) e^{-jk\xi} \quad (2.3a)$$

and

$$I(\xi, \omega) = \frac{V_o(\omega)}{Z_c} e^{-jk\xi} \quad (2.3b)$$

Note that the coordinate ξ is measured *along* the simulator plates as shown in Figure 2.3b, and is different from the x-coordinate in the launching and the termination sections.

The source term $V_o(\omega)$ can be approximated in terms of the measured electric field $E_o(\xi_o, \omega)$ in the working volume at a point $\xi = \xi_o$ as

$$V_o(\omega) = E_o(\xi_o, \omega) h e^{+jk\xi_o} \quad (2.4)$$

Here h is the working volume height of 40 m. The exponential in this equation contributes to a phase function, which amounts to a shift in the time domain of $\tau = \xi_o/c$. Thus, the time domain waveform of Figure 2-2a and the corresponding spectrum of Figure 2-2b represent the simulator excitation voltage, when multiplied by h and shifted by the appropriate time. In the development to follow, we assume that the $t = 0$ reference point occurs when the pulser first fires.

More general expressions for the source term $V_o(\omega)$ and the input impedance of the pulser Z_{in} can be developed for a line having an arbitrary load. However, these are not needed in the present case, due to the fact that the line is assumed to be perfectly matched.

2.3.3 Evaluation of The Radiated Fields.

To calculate the E- and H-fields radiated by the simulator, we need to integrate over the current distribution, as in Equation 2.2. To do this, the total current distribution can be represented by a distribution of electrically small current elements $I d\xi$ as shown in Figure 2-5. We use about current 10 elements per wavelength and compute the total radiated fields by summing over these current element contributions as an approximation to the continuous integral.

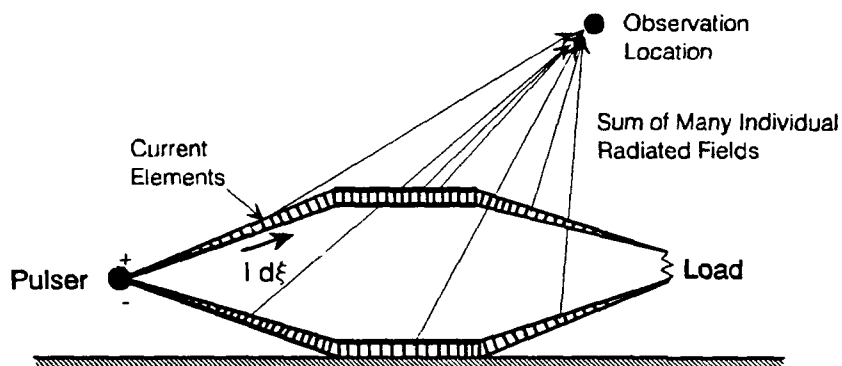


Figure 2-5. Discrete simulator current elements producing a radiated field.

The evaluation of the integral in Equation 2.2 requires a knowledge of the Green's dyad, $\bar{\bar{G}}(\vec{r}; \vec{r}')$. This may be obtained by computing the radiated fields produced by an infinitesimal current element located over a lossy earth, as shown in Figure 2-6. The EM field at the observer's location consists of 3 components: a direct wave, an earth-reflected wave, and a surface wave propagating along the earth-air interface [14]. Previous investigations into the behavior of these fields indicate that for both the current source and a distant observer positioned on or near the ground, the surface wave is the most important component. For the observer located well above the earth, the surface wave is negligible and the response is due mainly to the direct and earth-reflected fields.

The theoretical development for determining the fields from a current element has been described in references [14,15,16]. This theory is well-established and will not be re-derived here; only the results are summarized. For convenience in developing the expressions for the radiated fields from an arbitrarily oriented current element, the current is decomposed into a vertical and horizontal component. Generally, the vertical current element will radiate more efficiently in the presence of the ground than will the horizontal element. As most of the current on ARES is horizontal, it is expected that the radiation from the simulator will not be as large as for the case of a vertically polarized dipole (VPD) simulator. This view is consistent with the bounded field nature of ARES.

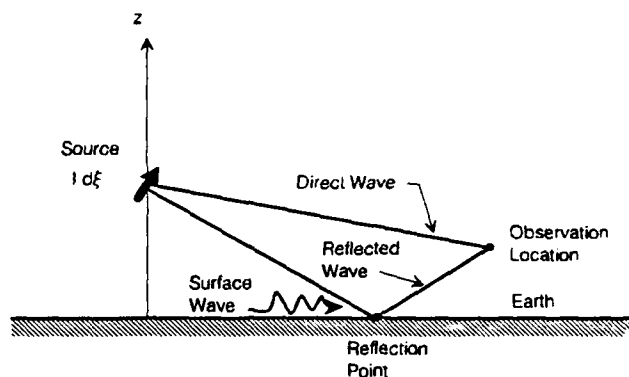


Figure 2-6. Field components produced by an infinitesimal current element over the earth.

2.3.3.1 E-field From a Vertical Current Element. Figure 2-7 illustrates the pertinent geometry for the E-field produced by a from vertical current element. Due to the azimuthal symmetry of the vertical current element, the fields are rotationally symmetric about the z axis. As discussed by Norton [15], the rigorous formulation for the E-fields produced by this current element is described by the formulation of Sommerfeld. This solution can be approximated by considering wave contributions directly from the current element, from a fictions "image" source in the ground with an appropriate multiplicative coefficient, and from a surface wave. It is known that as the earth becomes perfectly conducting, the surface wave term vanishes, and the image term becomes the normal image representing the reflection of the fields in the perfect ground.

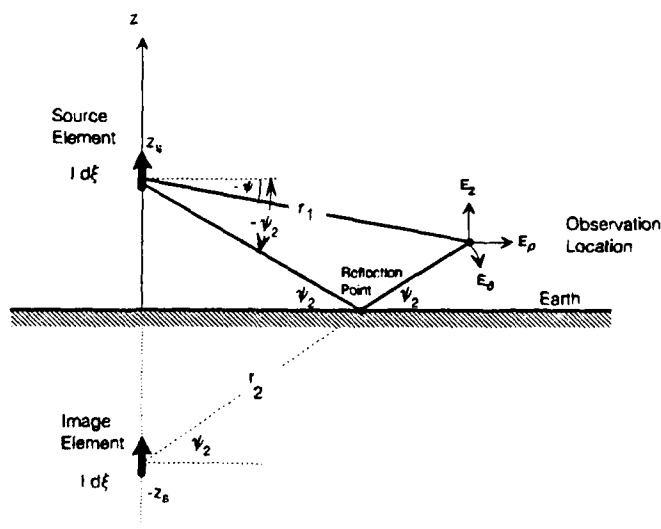


Figure 2-7. Geometry for a vertical current element.

The E-field components produced at an observer location by the direct and image sources are most suitably expressed in cylindrical coordinates (ρ, ϕ, z) . These are given in [14] as

$$E_z = -j 30k Id\xi \left[\cos^2 \psi_1 \frac{e^{-jkr_1}}{r_1} + R_v \cos^2 \psi_2 \frac{e^{-jkr_2}}{r_2} \right] \quad (2.5a)$$

and

$$E_\rho = j 30k Id\xi \left[\cos \psi_1 \sin \psi_1 \frac{e^{-jkr_1}}{r_1} + R_v \cos \psi_2 \sin \psi_2 \frac{e^{-jkr_2}}{r_2} \right] \quad (2.5b)$$

In these expressions, the terms r and ψ represent the distance and the wave-path angles for the primary current element and for its image, as indicated in Figure 2-7. In developing these equations, it is assumed that the frequency is sufficiently high so that $kr = \omega r/c \gg 1$, and the static and quasi-static (induction) fields are neglected. Thus, only the $1/r$ radiation fields are retained.

For a transient analysis using a FFT, it is clear that there will be some frequencies in the wide-band spectrum that are too low for the above approximation to be valid. For example, for an observer at $r = 500$ m, the frequency at which $kr = 10$ is about 955 kHz. Below this frequency, the use of only the far-field radiation component is not strictly justified. With reference to the ARES excitation spectrum of Figure 2-2b, it is seen that there are several frequency points in this region and the calculations will be in error there. In the time domain, however, this low-frequency error in the spectral response translates to errors in the late-time waveform, or possibly to a dc baseline shift. Many times we are more interested in the early-time waveform attributes, such as the rise time or the peak value. Low frequency spectral errors have been seen to have a negligible effect on these parameters in most cases, especially for the fields far from the simulator.

The term R_v in Equation 2.5 is the Fresnel reflection coefficient for vertical polarization which is expressed in [17] as

$$R_v = \frac{\epsilon_g \left(1 + \frac{\sigma_g}{j\omega\epsilon_g\epsilon_o} \right) \sin \psi_2 - \sqrt{\epsilon_g \left(1 + \frac{\sigma_g}{j\omega\epsilon_g\epsilon_o} \right) - \cos^2 \psi_2}}{\epsilon_g \left(1 + \frac{\sigma_g}{j\omega\epsilon_g\epsilon_o} \right) \sin \psi_2 + \sqrt{\epsilon_g \left(1 + \frac{\sigma_g}{j\omega\epsilon_g\epsilon_o} \right) - \cos^2 \psi_2}} \quad (2.6)$$

The parameter σ_g is the earth conductivity, ϵ_g is the relative earth dielectric constant, and ϵ_0 is the free-space dielectric constant of 8.854×10^{-12} (F/m). Note that the angle ψ_2 corresponds to a plane-wave incidence angle at a specular reflection point, as indicated in Figure 2-7.

The approximate expressions for the Norton surface wave components of the E-field are summarized in reference [14] as

$$E_z = -j 30k Id\xi \left[(1-R_v) (1-u^2 + u^4 \cos^2 \psi_2) F(\chi) \frac{e^{-jkr_2}}{r_2} \right] \quad (2.7a)$$

and

$$E_\rho = -j 30k Id\xi \left[(1-R_v) u \sqrt{1-u^2 \cos^2 \psi_2} \left(1 + \frac{\sin^2 \psi_2}{2} \right) F(\chi) \frac{e^{-jkr_2}}{r_2} \right] \quad (2.7b)$$

In these equations, $u^2 = 1/(\epsilon_g - j(\sigma_g / \omega \epsilon_0))$, $F(\chi) = 1 - j\sqrt{\pi\chi} e^{-\chi} \text{erfc}(j\sqrt{\chi})$, and the parameter χ is

$$\chi = \frac{-jkr_2 u^2 (1-u^2 \cos^2 \psi_2)}{2} \left[1 + \frac{\sin \psi_2}{u \sqrt{1-u^2 \cos^2 \psi_2}} \right]^2 \quad (2.8)$$

2.3.3.2 E-field From a Horizontal Current Element. The E-fields radiated by a horizontal current element are slightly more complicated, due to the absence of symmetry about the z axis. As shown in Figure 2-8, the fields will depend on the cylindrical angle ϕ . For this horizontal source, the E-field components are expressed in Cartesian coordinates. For the current element assumed to be directed along the x axis, the three components of the direct and image radiation-zone E-fields are

$$E_z = j 30k Id\xi \cos \phi \left[\sin \psi_1 \cos \psi_1 \frac{e^{-jkr_1}}{r_1} - R_v \sin \psi_2 \cos \psi_2 \frac{e^{-jkr_2}}{r_2} \right] \quad (2.9a)$$

$$E_x = -j 30k Id\xi \left[\cos^2 \phi \left(\sin^2 \psi_1 \frac{e^{-jkr_1}}{r_1} - R_v \sin^2 \psi_2 \frac{e^{-jkr_2}}{r_2} \right) + \sin^2 \phi \left(\frac{e^{-jkr_1}}{r_1} + R_h \frac{e^{-jkr_2}}{r_2} \right) \right] \quad (2.9b)$$

$$E_y = -j 30k I d\xi \sin \varphi \cos \varphi \left[\left(\sin^2 \psi_1 \frac{e^{-jkr_1}}{r_1} - R_v \sin^2 \psi_2 \frac{e^{-jkr_2}}{r_2} \right) + \left(\frac{e^{-jkr_1}}{r_1} + R_h \frac{e^{-jkr_2}}{r_2} \right) \right] \quad (2.9c)$$

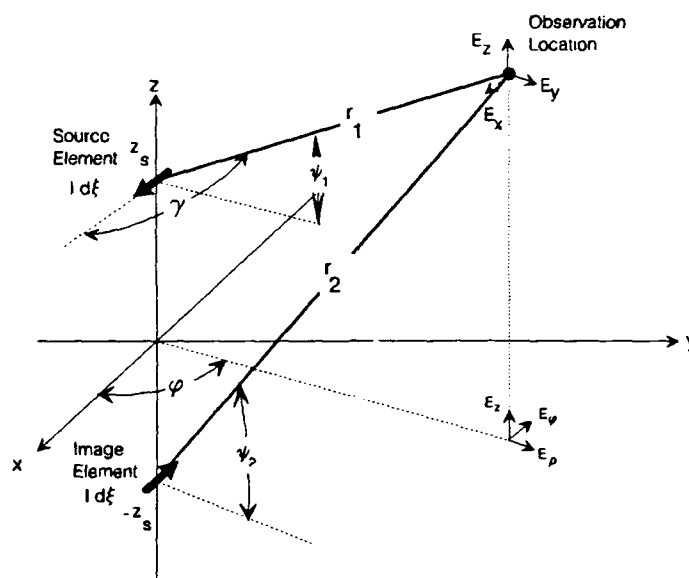


Figure 2-8. Geometry for a horizontal current element.

In addition to the vertically polarized reflection coefficient, R_v , defined previously, these expressions also use a horizontally polarized reflection coefficient, R_h , of the form [17],

$$R_h = \frac{\sin \psi_2 - \sqrt{\epsilon_g \left(1 + \frac{\sigma_g}{j\omega\epsilon_g\epsilon_o} \right) - \cos^2 \psi_2}}{\sin \psi_2 + \sqrt{\epsilon_g \left(1 + \frac{\sigma_g}{j\omega\epsilon_g\epsilon_o} \right) - \cos^2 \psi_2}} \quad (2.10)$$

The corresponding Norton surface wave contribution to the E-fields for this current element is also expressed in terms of cylindrical coordinates. Reference [14] gives these fields as

$$E_z = j 30k Id\xi \left[\cos \varphi u \sqrt{1-u^2 \cos^2 \psi_2} (1-R_v)(1-u^2 + u^4 \cos^2 \psi_2) F(\chi) \frac{e^{-jkr_2}}{r_2} \right] \times \cos \psi_2 \left(1 + \frac{\sin^2 \psi_2}{2}\right) \quad (2.11a)$$

$$E_\rho = j 30k Id\xi \left[\cos \varphi u \sqrt{1-u^2 \cos^2 \psi_2} (1-R_v)(1-u^2 + u^4 \cos^2 \psi_2) F(\chi) \frac{e^{-jkr_2}}{r_2} \right] \times u \sqrt{1-u^2 \cos^2 \psi_2} \left[\frac{1 - \sin^2 \psi_2 - \frac{(1-R_h)}{(1-R_v)u^2} \frac{F(\chi')}{F(\chi)}}{1-u^2 \cos^2 \psi_2} \right] \quad (2.11b)$$

$$E_\varphi = j 30k Id\xi \left[\cos \varphi u \sqrt{1-u^2 \cos^2 \psi_2} (1-R_v)(1-u^2 + u^4 \cos^2 \psi_2) F(\chi) \frac{e^{-jkr_2}}{r_2} \right] \times \sin \varphi (1-R_h) F(\chi') \quad (2.11c)$$

The terms k , u , ξ , $F(\chi)$, and R_v have been defined previously for the surface wave in Equation 2.7. In Equation 2.11, the parameter χ' is given by

$$\chi' = \frac{-jkr_2 (1-u^2 \cos^2 \psi_2)}{2u^2} \left[1 + \frac{\sin \psi_2}{u \sqrt{1-u^2 \cos^2 \psi_2}} \right]^2 \quad (2.12)$$

2.3.3.3 Simplifications for the Radiated Field. One of the difficulties in evaluating Equation 2.2 by a direct numerical integration is that at high frequencies, many discrete current elements are needed to adequately represent the integral. For example, at 60 MHz where the wavelength $\lambda = 5$ meters, current elements with a length $\lambda/10 \approx 0.5$ meters are required. To compute the fields radiated from both the top and bottom plate currents, this requires about 775 segments. At 90 MHz, the required number of elements increases to over 1150. Because

these calculations must be performed for many different frequencies to ultimately perform the inverse FFT for the transient response, very long computer times can be expected for these calculations.

In some cases it is possible to simplify integration in Equation 2.2. For cases when the observation location is located far above the ground so that the surface wave contribution is negligible compared to the sky-wave and reflected wave, considerable computational savings can result from not having to evaluate functions $F(\xi)$ and $F(\xi')$. Furthermore, if the observation point is also sufficiently far from the simulator so that $|\bar{r}| \gg L$, where L is the longest simulator dimension, Equation 2.2 reduces simply to integrations of exponential functions which may be evaluated analytically. This is analogous to Fresnel diffraction theory [14].

As a consequence of these simplifications, the radiated E-field components for distant airborne locations can be computed by simply adding six analytical contributions from each of the six wire segments, as shown in Figure 2-9. The ground interaction of these currents must also be considered, and this amounts to considering another six image current segments in the earth. Thus, for any frequency, only 12 terms are summed to compute the radiated field. This results in a dramatic savings in the computer time for these airborne field points.

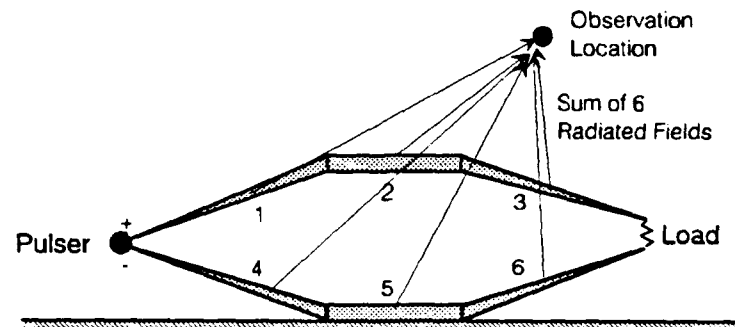


Figure 2-9. Simplification of the integration process for distant, airborne observation points.

To determine the fields produced by one of the finite-length current elements (or their images) in Figure 2-9, the solution to the canonical radiation problem shown in Figure 2-10 can be used. This is an isolated, straight vertical wire segment of length L , carrying a positive traveling wave current of the form

$$I(z) = I_0 e^{-jkz} \quad (2.13)$$

At frequencies such that $kr \gg 1$, the far-field radiation produced by this line segment consists of only a E_θ component [18], and for $r \gg L$, this can be expressed as

$$E_\theta = j30k \sin \theta I_0 \frac{e^{-jkr_0}}{r_0} \int_0^L e^{-jk\xi} e^{jk\xi \cos \theta} d\xi. \quad (2.14)$$

The integral in Equation 2.14 can be integrated analytically to give

$$E_\theta = -30 \sin \theta I_0 \frac{e^{-jkr_0}}{r_0} \frac{(e^{-jk(1-\cos \theta)L} - 1)}{(1 - \cos \theta)}. \quad (2.15)$$

A similar expression can be developed for a negative traveling current wave of the form $I(z) = I_0 e^{+jkz}$, but this is not necessary because the load impedance matching on ARES implies that only forward traveling waves exist on the simulator.

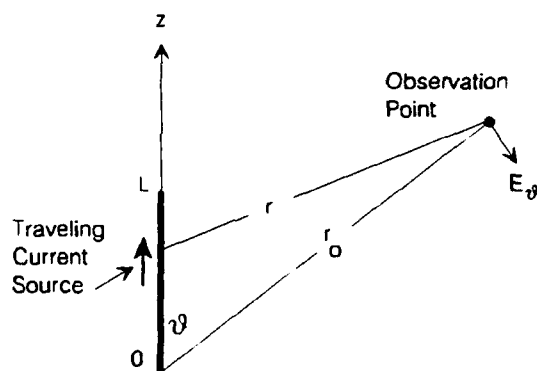


Figure 2-10. Geometry for calculating the radiated fields from a wire segment of length L .

The actual directions of the current elements in Figure 2-9 are not vertical, so the resulting field in Equation 2.15 must be modified. This is done by rotating the z -directed current element to align with the direction of the actual current and then evaluating the rotated E_θ field in the Cartesian system. The details of this procedure are standard, and will not be presented here. Furthermore, the fields produced by the image sources must be modified by the Fresnel reflection coefficients to account for the imperfect ground.

2.3.3.4 Determination of the Magnetic Field. The previous discussion has been made with the E-field taken as the principal observation quantity. The magnetic field is also of interest, especially since the experimental programs usually have measured H. The evaluation of explicit expressions for the H-field from the sky and earth-reflected wave components is a relatively easy task. However, the determination of the H-field for the surface wave is more difficult. In fact, explicit expressions for the H-field surface waves have not been found in the literature. While it is possible to develop such expressions for this H-field component, an alternative approach is to evaluate the total H-field from a knowledge of the E-field and the Maxwell equation

$$\nabla \times \vec{E} = -j\omega\mu\vec{H} . \quad (2.16)$$

In Cartesian coordinates, the individual field components are

$$H_x = \frac{j}{\omega\mu} \left[\frac{\partial E_z}{\partial y} - \frac{\partial E_y}{\partial z} \right] \quad (2.17a)$$

$$H_y = \frac{j}{\omega\mu} \left[\frac{\partial E_x}{\partial z} - \frac{\partial E_z}{\partial x} \right] \quad (2.17b)$$

$$H_z = \frac{j}{\omega\mu} \left[\frac{\partial E_y}{\partial x} - \frac{\partial E_x}{\partial y} \right] . \quad (2.17c)$$

Thus, the H-field can be determined from the spatial derivatives of the E-field. From a numerical standpoint, this involves representing these derivatives by a finite difference operator, which requires separate evaluations of the E-field at different spatial locations to compute the H-field. Note that as $\omega \rightarrow 0$ the expressions in Equation 2.17 become undefined. This suggests that at low-frequencies the evaluation of the H-fields will contain errors, due to the numerical evaluation process. These errors, however, appear most noticeably at late times in the transient response, and consequently, do not significantly affect the early-time peak responses.

SECTION 3

MODEL VALIDATION

It is important to validate the accuracy of the formulation and the numerical implementation of this model. There are several ways of doing this, including a direct comparison with experimental data and the careful examination of the transient radiated field waveform characteristics. The results of both such checks are discussed in this section.

3.1 FIELD MEASUREMENTS ON THE GROUND.

An experimental program described in reference [8] resulted in the measurement of the three vector components of the H-field at different ground locations away from ARES. These points were located at distances between 1.9 to 3.3 km from the simulator. The vector components of the measured H-fields consisted of a radial component, a vertical component, and a component perpendicular to the two, which is parallel to the earth. These are shown in Figure 3-1 as H_ρ , H_z , and H_ϕ . For the surface wave propagating away from ARES, the H_ϕ component is usually the largest.

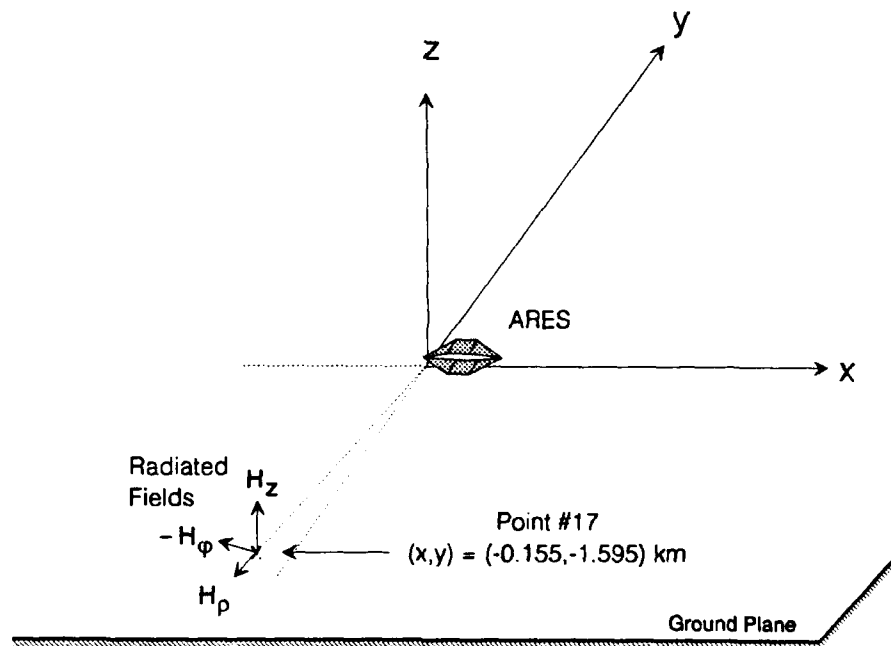
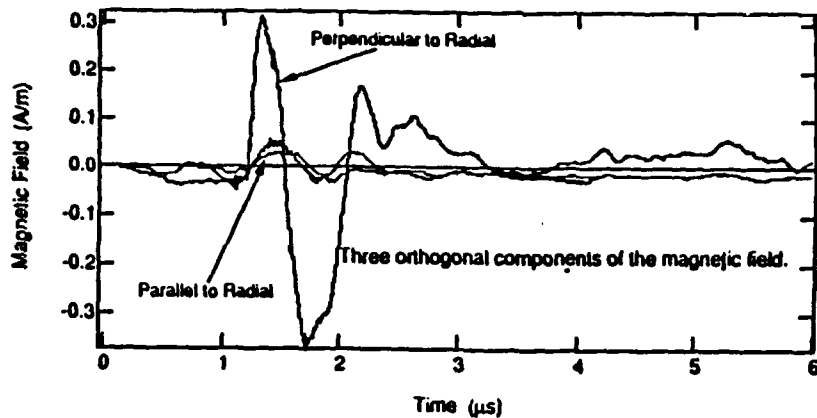
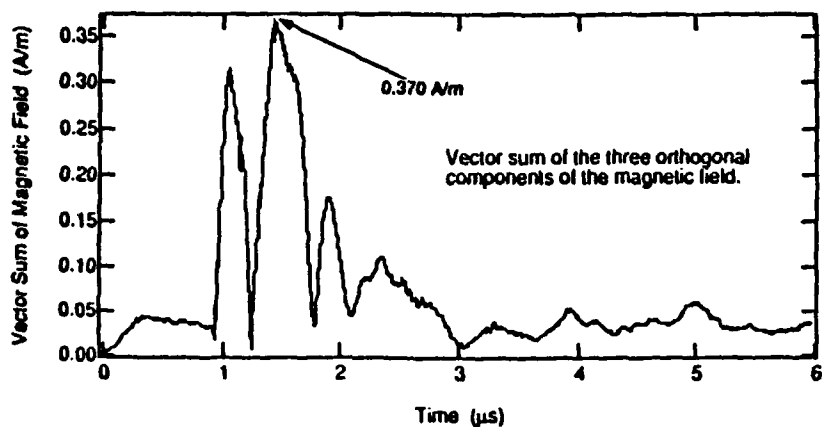


Figure 3-1. Radiated fields on the ground away from ARES.

For observation location #17, defined by the (x,y,z) coordinates of $(-0.155, -1.595, 0.0)$ km, the measured transient H-field waveform components from [8] are shown in Figure 3-2a. Figure 3-2b presents the magnitude of the total transient H-field, defined formally as $|H(t)| = \sqrt{H_p^2(t) + H_q^2(t) + H_z^2(t)}$. At this location, the overall peak H-field was 0.37 (A/m).



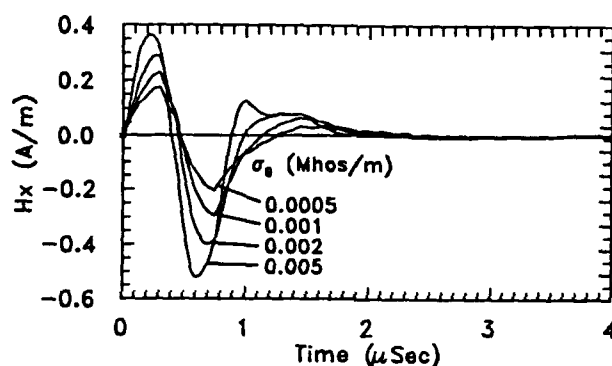
(a) H-field components



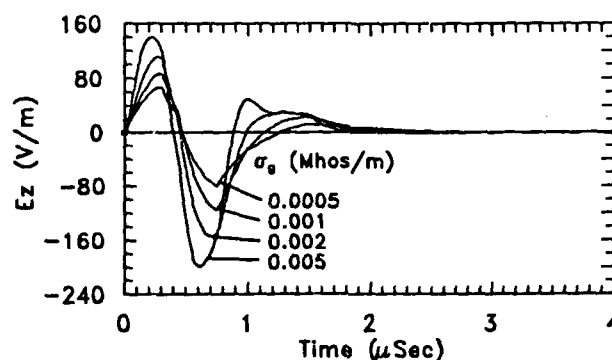
(b) Total H-field

Figure 3-2. Measured H-field at location #17, from [8].

As shown in Figure 3-2, point #17 is located almost due south of ARES. As a result, the principal H-field component is almost completely parallel to ARES (i.e., in the x direction). Thus, the measured principal component can be compared with the computed x-component of the H-field radiating from the simulator. Figure 3-3a presents the calculated H_x field components at location #17 for a set of different earth conductivities, ranging from $\sigma_g = 0.0005$ to 0.005 S/m. Figure 3-3b illustrates the corresponding principal E_z field component at point #17. Because the earth conductivity varies with the water content of the soil and is not accurately known, it is necessary to determine a reasonable value for this parameter. A good comparison between the measured and calculated H-fields, both in amplitude and waveshape, is obtained for an earth conductivity in the range of 0.002 to 0.005 S/m. Based on this comparison, the earth conductivity for the remainder of this study is taken to be $\sigma_g = 0.003$ S/m. This value is close to the value of 0.002 S/m estimated by DNA.



(a) H_x field component



(b) E_z field component

Figure 3-3. Calculated principal H- and E-field components at point # 17.

With the above selected value of earth conductivity, field calculations in a 10×10 km region surrounding ARES were performed. Contours of the resulting peak transient H-fields are plotted in Figure 3-4. The contours in this plot represent lines of constant peak H-field in A/m. Also shown on this figure are the locations of the test points from [8], along with the maximum and minimum measured values. As may be noted from this figure, the agreement between the experimental and calculated results is excellent.

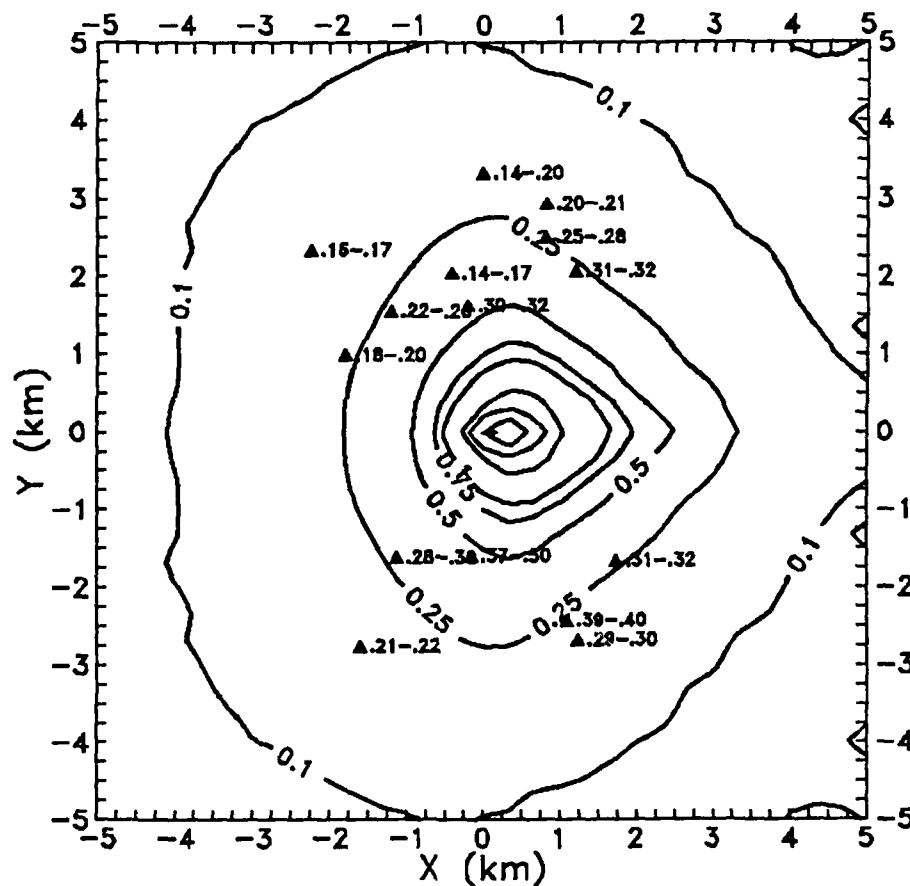


Figure 3-4. Contours of total peak H-field in A/m on the ground (experimental points from [8] are marked by Δ).

Although the corresponding E-field was not measured, its behavior is of interest. Figure 3-5 illustrates computed contours of constant E-field peak values (in V/m) on the ground around ARES. This E-field is principally in the vertical (z) direction.

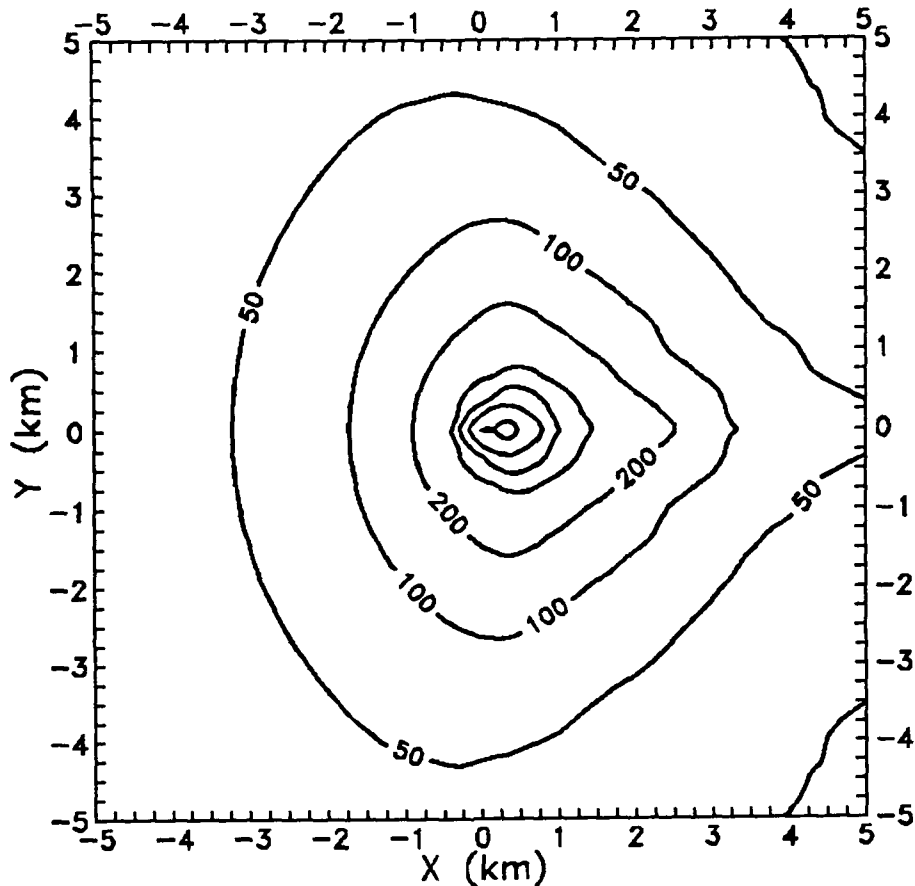


Figure 3-5. Contours of total peak E-field in V/m on the ground.

It should be noted that the calculations for Figures 3-4 and 3-5 used 264 unique observation locations within the region $-5 \leq x \leq 5$ and $0 < y \leq 5$ km. The locations of these points were randomly chosen within the region, and this resulted in a uniform distribution of field points. Due to the symmetry of the simulator geometry, the fields for $y < 0$ were inferred from the fields for $y > 0$. Obtaining the data for these plots required approximately 176 hours of computer time on a 80386/80387 33 MHz PC. More details on the calculational requirements for this model are provided in Section 7.

3.2 FIELD MEASUREMENTS IN THE AIR.

Fields measured at an observation location in the air provide an alternate way of validating the model. In December, 1991, DNA conducted a field test with an airborne B-dot measurement system to acquire such data [19]. Unfortunately, due to equipment malfunctions, a measurement at only one location was obtained. The measured peak H-field components are shown in Table 3-1. Also shown in the table are the corresponding calculated H-field quantities. Due to the motion of the measurement equipment, the x-y-z coordinate axes of the B-dot sensors may not have been aligned precisely with the x-y-z coordinates of the simulator. Thus, the vector sum of the H-field components is a more accurate measure for comparison purposes. The total H-fields agree to within about 7 %. The corresponding total E-field at this location is computed assuming a plane wave relationship between E and H. This gives $E_{tot} = 377 H_{tot} = 110.4 \text{ V/m}$. Figure 3-6 presents a plot of the total transient H-field magnitude computed for this observation location.

Table 3-1. Peak H-field components at $(x,y,z) = (-1025, -1617, 61) \text{ m}$.

H-Field Component	Measured Peak Value (A/m)	Computed Peak Value (A/m)
H_x	0.245	0.228
H_y	0.157	0.150
H_z	0.032	0.021
H_{tot}	0.293	0.273

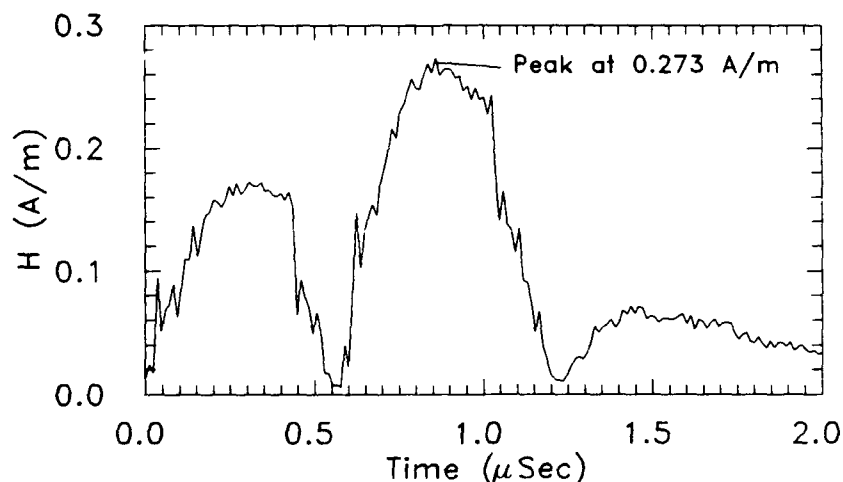


Figure 3-6. Plot of the calculated total transient H-field magnitude at $(x,y,z) = (-1025, -1617, 61) \text{ m}$.

3.3 INVESTIGATION OF WAVEFORM CHARACTERISTICS.

Another method for validating the ARES analysis is to examine features of the radiated waveform and check that the various times of arrival of its components are correct. For a distant observation point $(x,y,z) = (10,10,10)$ km, Figure 3-7 shows an example of the radiated E_z field component using an assumed perfectly conducting earth. This waveform contains time-of-arrival information relating to various parts of the simulator structure. However, these are masked by the pulser waveform variations that are shown in Figure 2-2a.

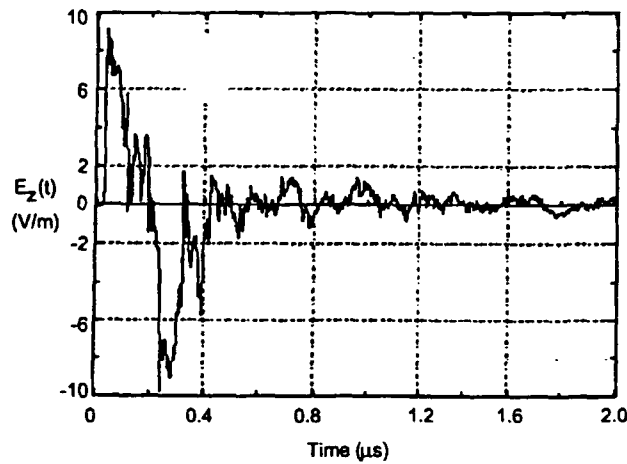
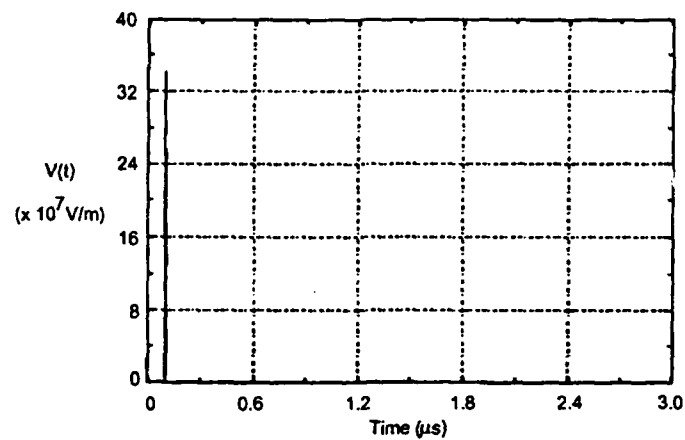
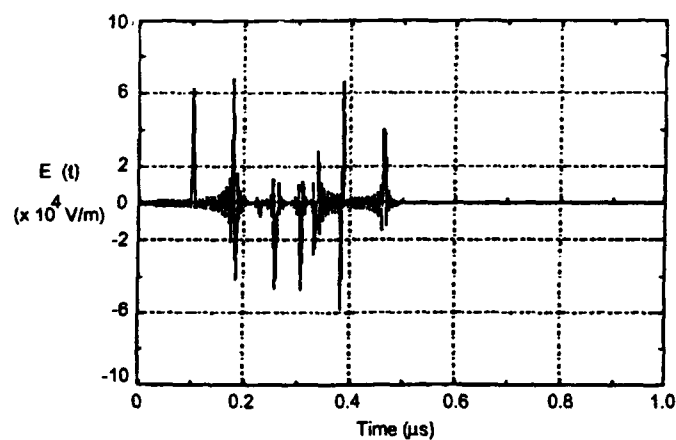


Figure 3-7. Radiated E_z field at $(x,y,z) = (10,10,10)$ km.

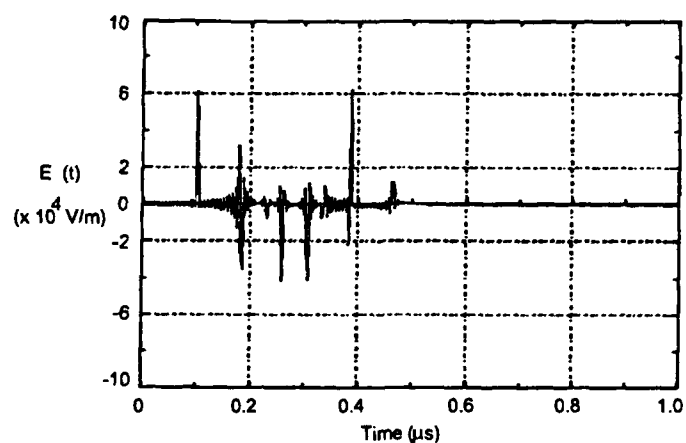
To see these waveform features more clearly, it is useful to consider the impulse response of the simulator. Figure 3-8a shows a numerical approximation to a unit impulse shifted in time to start at $t = 0.1 \mu\text{s}$. The computed E_z component of the radiated field at $(x,y,z) = (10,10,10)$ km for this excitation is shown in Figure 3-8b for a perfectly conducting earth. Figure 3-8c shows the same radiated E-field component for a lossy earth with $\sigma_g = 0.003 \text{ S/m}$. The actual radiated field shown in Figure 3-7 is the convolution of this impulse response and the excitation waveform of Figure 2-2a.



(a) Delta function excitation



(b) E_z response for perfect ground



(c) E_z response for lossy ground

Figure 3-8. ARES impulse excitation (a) and radiated E_z field responses (b) and (c) at $(x,y,z) = (10, 10, 10)$ km.

The radiated impulse response waveform of Figure 3-8b contains individual components arising from discontinuities in the current flow on the simulator. For a uniform segment of current, as shown in Figure 2-10, Equation 2.15 indicates that there will be a far-field radiation contribution arising from each end of the segment where there is a discontinuity in the flow of current. Thus, with reference to Figure 3-9, the radiation field at point O will consist of contributions arriving from simulator discontinuity points A, A', B, B', C, C', etc. Because the contribution from each of the ray-paths varies as point O moves, the radiated waveform shape will vary as a function of the observation location.

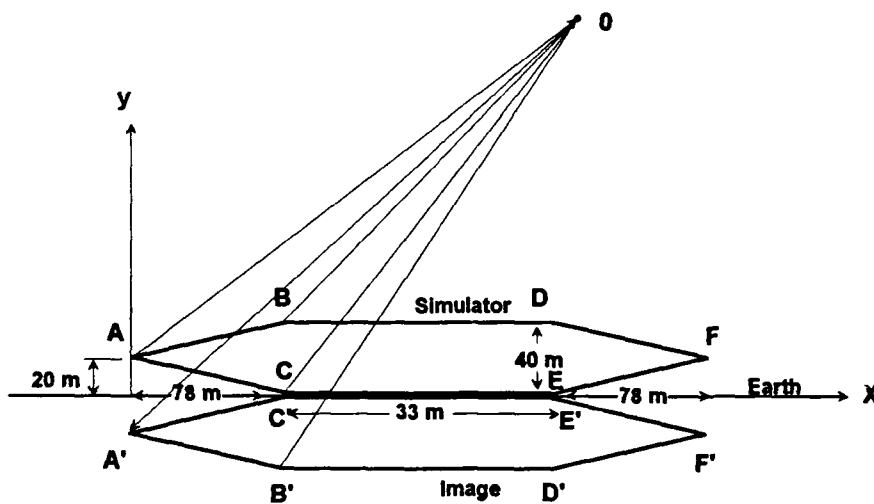


Figure 3-9. Waveform contributions at point O.

That the waveform in Figure 3-8b is reasonable can be determined by examining the times of arrival of the various impulses. The first impulse at $t \approx 0.1 \mu\text{s}$, arrives by the direct path from the pulser source to the observer, (A-O). The second impulse is due to a wave traveling from (A-B) and then from (B-O). The time difference between the arrival of the first and second responses is given by $[(A-B)+(B-O)-(A-O)]/c = 0.077 \mu\text{s}$, and this is clearly indicated in the figure. A careful examination of the times of arrival of the other waveform features has been performed, and the model has been shown to be providing the correct response times.

SECTION 4

NUMERICAL RESULTS

With the ARES calculational model validated, a series of numerical experiments was conducted to illustrate the behavior of the EM fields around the simulator. The results are presented in this Section.

4.1 TRANSIENT FIELDS ON THE GROUND.

For ground observation locations very close to the simulator, TEM field models suggest that the radiated fields will be roughly 10% to 30 % of the working volume fields. Furthermore, these fields should exhibit a significant amount of detail in the waveshape, as in Figure 2-2a. However, as the observation location moves away from the simulator, the $1/r$ fall-off of the fields produced by the simulator currents and the additional attenuation of the Norton surface wave causes the field amplitude to drop. Also, because the high frequency components of the waveform attenuate more rapidly with distance than the low frequency components, it is expected that the radiated waveform will become smoother at large distances on the ground.

Figure 4-1 shows the behavior of the three components of the transient H-field for several different locations due north of the center of the ARES working volume. These positions are given by $(x,y,z) = (94.5, y, 0)$ m, where y varies from 50 m to 5 km. Note that for this calculation, the earth conductivity was taken to be $\sigma_g = 0.002$ S/m instead of the value of 0.003 S/m. These fields behave as expected, with the H_x component being the primary field component far away from the simulator. Notice that each of the ordinate scales is different in Figure 4-1. Figure 4-2 presents similar data for the E-field behavior at the same observation locations.

4.2 DEPENDENCE OF GROUND FIELDS ON RANGE.

The calculated field data at the spatial points for Figures 3-4 and 3-5 are replotted as a function of their ground range in Figures 4-2a and b. In addition to a radial dependence of these fields, there is an angular variation of the fields. Because the field observation locations are at different angles ϕ , these curves are not smooth. However, they do give an indication of the average field behavior as the distance is increased. Also plotted in these figures is a $1/r$ function, which clearly illustrates that these fields fall off faster than $1/r$. This is due to the more rapid attenuation of the Norton surface wave.

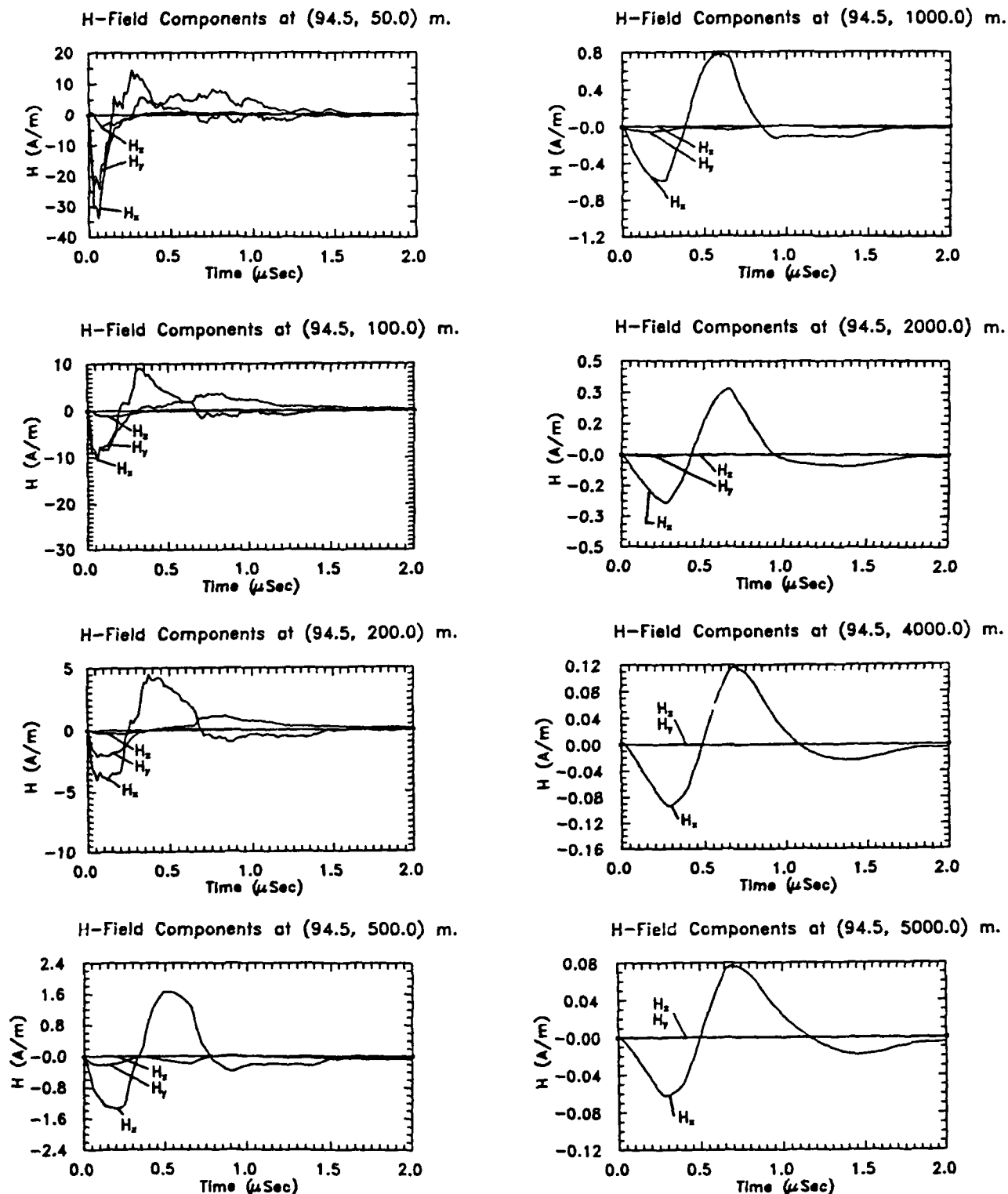


Figure 4-1. Plots of the transient H-field components on the ground to the North of ARES.

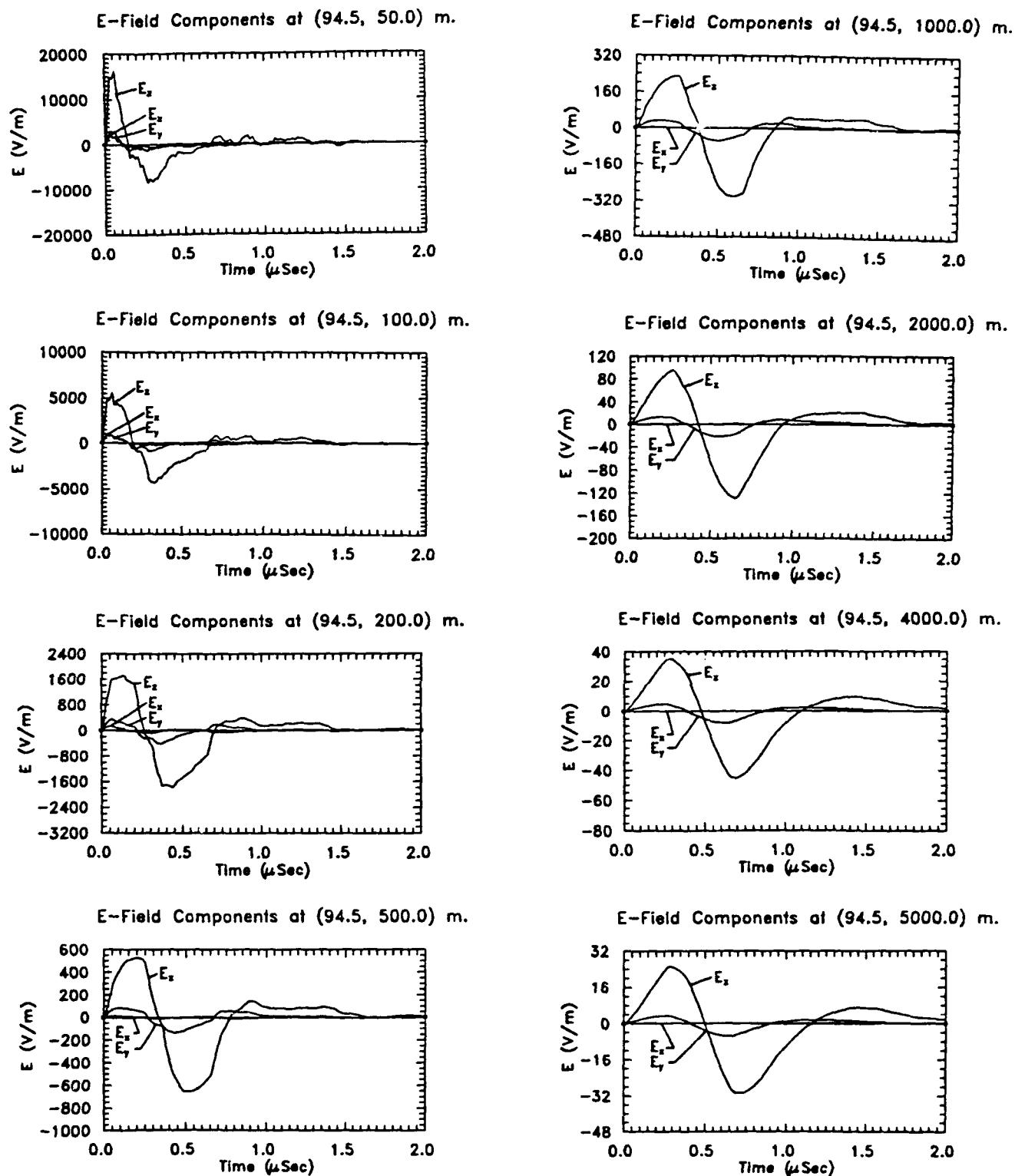
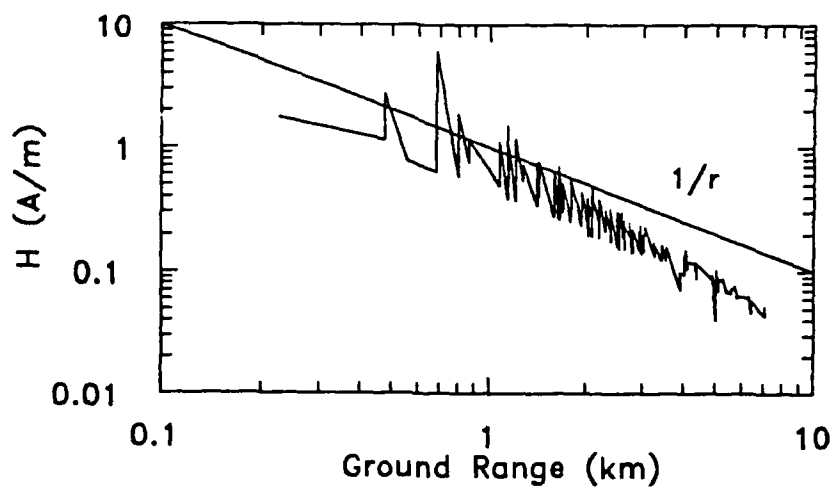
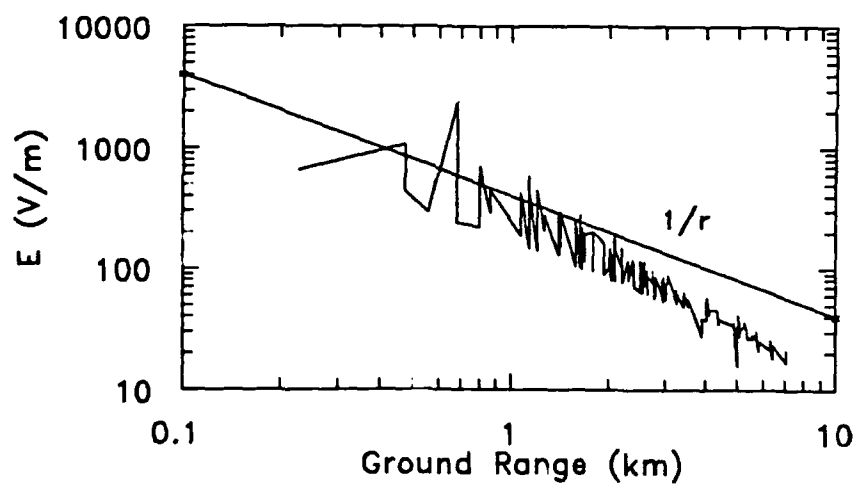


Figure 4-2. Plots of the transient E-field components on the ground to the North of ARES.



(a) H-field



(b) E-field

Figure 4-3. Variations of peak transient fields with range.

4.3 IMPORTANCE OF THE SURFACE WAVE.

The Norton surface wave is essential for an accurate solution for the fields on the ground. As discussed in [14], for a point current source and an observer located on a lossy earth the direct and earth-reflected contributions to the field tend to cancel. This gives only the surface wave as the main contributor to the response. For ARES, not all of the incremental current sources are located exactly on the earth, so this observation is not strictly true. However, it still is approximately correct, that far from the simulator, the ground fields are due mainly to the surface wave.

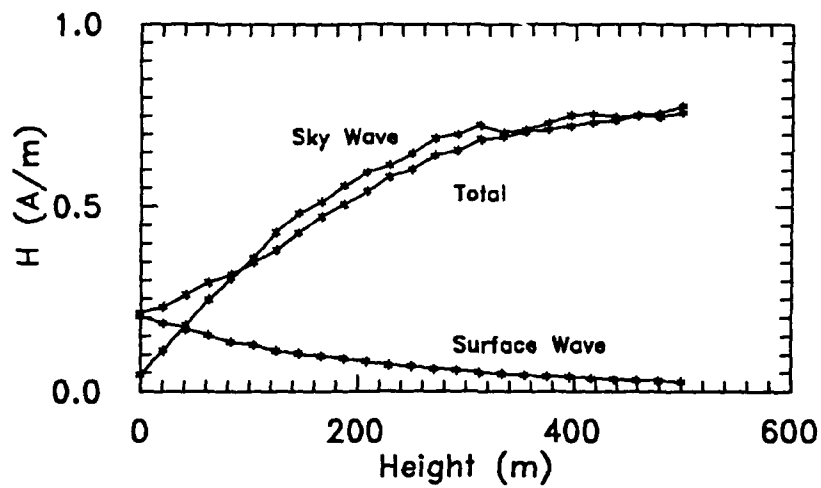
To understand the importance of this effect, a study of the composition of the radiated fields as a function of the observer height was conducted. An observer location of $(x,y,z) = (2, 2, z)$ km was chosen, with z varying from 0 to 500 m. Three different calculations of the peak H- and E-fields were made:

1. A complete solution containing all wave contributions,
2. A partial solution containing only the direct and earth-reflected wave contributions, given by Equations 2.5 and 2.9 (i.e., without the surface wave contributions),
3. A partial solution containing only the surface wave contributions, given by Equations 2.7 and 2.11.

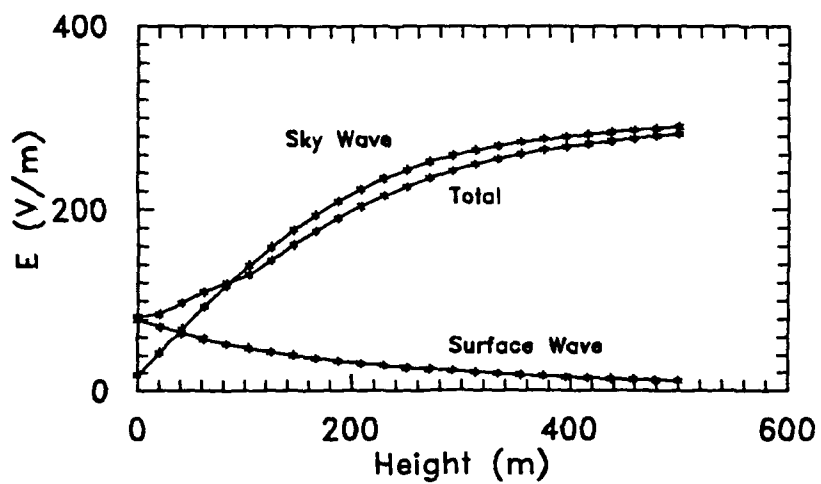
The resulting H- and E-field peak values are plotted as a function of the height in Figure 4-4. In this figure, the above three cases are labeled as "total", "sky wave", and "surface wave", respectively. This plot illustrates that for heights above 100 meters or so, the surface wave plays an unimportant role in determining the total field amplitudes. On the ground, however, its importance is clearly evident.

4.4 TRANSIENT E-FIELDS ABOVE THE GROUND.

As discussed in Section 3.3, the shape of the radiated waveform above the ground will vary depending on the relative positions of the scattering centers of the simulator. Figure 4-5 presents plots of the E_θ component of the far-field waveform calculated for a airborne observer at a constant radial distance of 20 km from ARES. With reference to Figure 2-3a, the angle ϕ is 0° and the values of θ are 30° , 60° , and 85° . In these plots, the turn-on time of the pulser has been shifted slightly so that the early-time portion of the waveform can be easily seen. Note again that the ordinates of these plots are different. At this distance, the corresponding H-field component is given by $H_\phi(t) = E_\theta(t)/377$.



(a) H-field peak value



(b) E-field peak value

Figure 4-4. Plots of the peak transient H- and E-fields for different heights at $(x,y) = (2, 2)$ km.

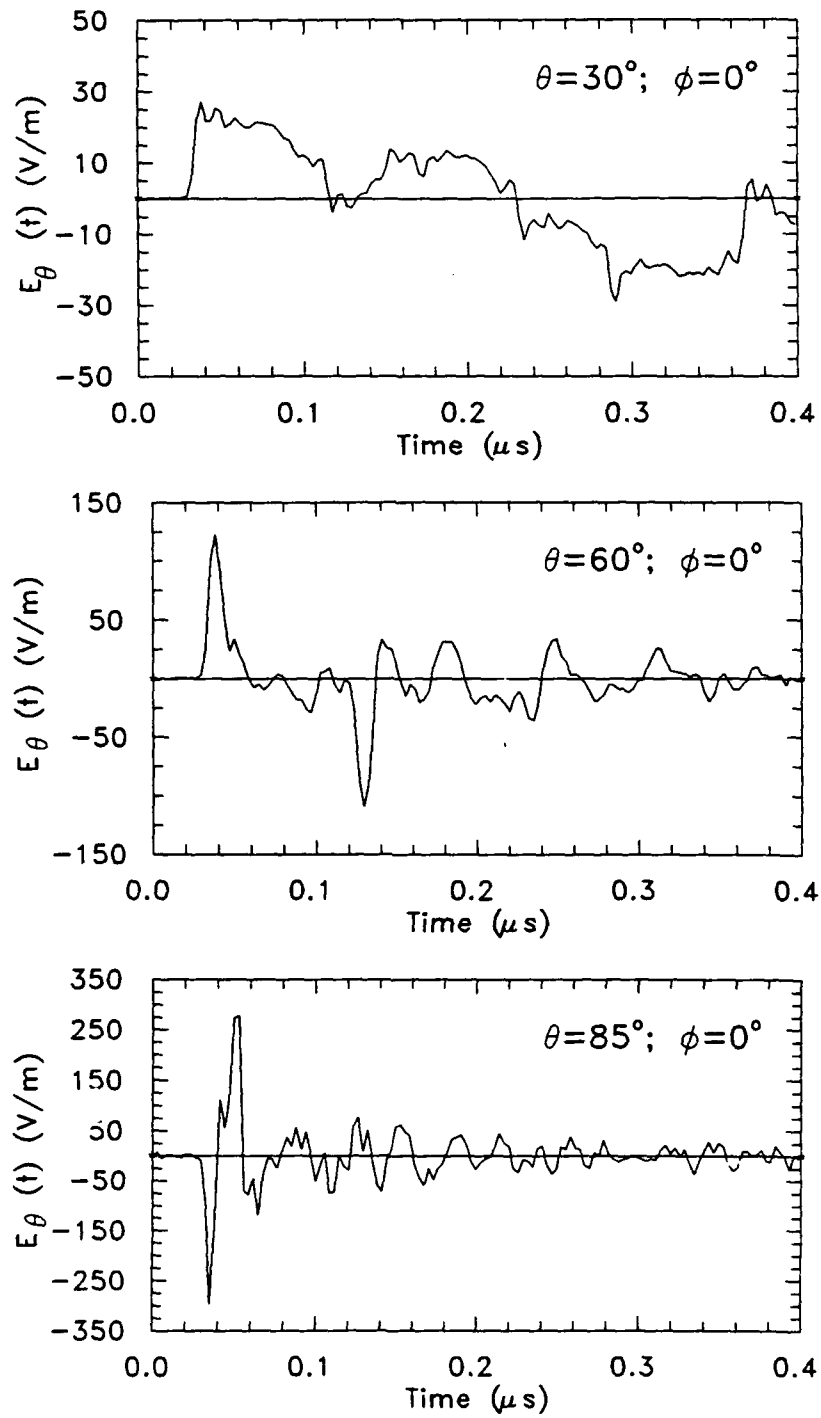


Figure 4-5. Far-field E_θ component of ARES for an airborne observer at $r = 20$ km and different values of the angle, θ .

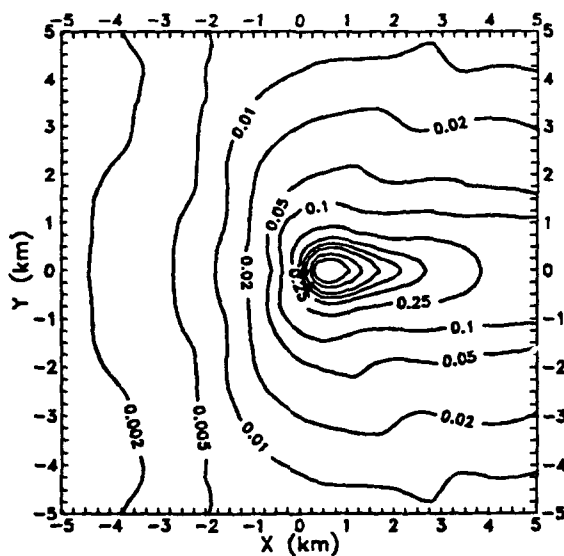
Note that as the angle θ becomes larger and the observation location comes closer to the earth, the radiated field waveform changes its shape. It appears to change from a series of more or less broad pulses to a waveform containing impulsive (delta function) contributions. As mentioned earlier this behavior is related to the different times of arrival of field contributions from the simulator diffraction points A, B, A', B', etc. in Figure 3-9 coinciding to produce the sharp peak in the radiated field in the end-fire direction. This same behavior is noted in the transient radiation pattern from a simple traveling-wave Beverage antenna.

4.5 SPATIAL PATTERN OF PEAK FIELDS IN THE AIR.

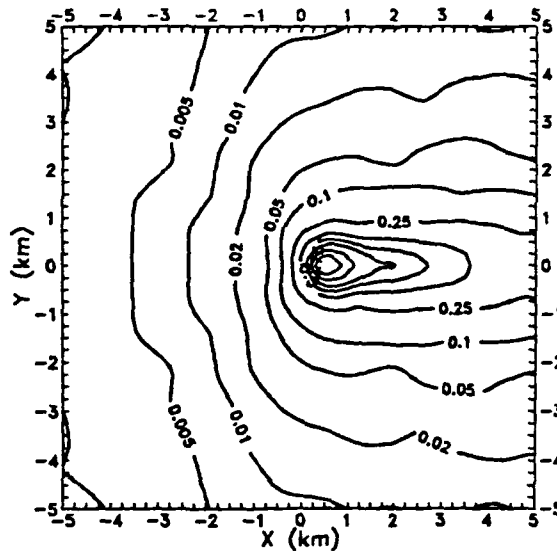
Spatial field maps of the peak H- and E-fields have also been calculated to provide an idea of the variations in the radiated fields in the air. These plots can be thought of as being similar to the field plots on the ground. Figure 4-6 shows the contours of the maximum H-fields (in A/m) at altitudes of 50, 100, 250, and 200 meters. Figure 4-7 shows the E-field peak data in a similar fashion. In both of these plots, the general trend of the fields increasing near the termination end of ARES is evident.

An alternate way of understanding the behavior of the fields in the space above the simulator is to use a 3-dimensional plot, similar to that of a radiation pattern. In such a plot, the peak transient E or H-field in a particular angular direction specified by the coordinate pair (θ, ϕ) is represented by the distance of a surface element from the origin. This is shown in Figure 4-8 for several different view angles. In computing this plot, the fields were evaluated at a constant radial distance of 20 km from the simulator, and the presence of the surface wave was neglected. As a consequence, radiated E and H are simply related by the impedance of free space.

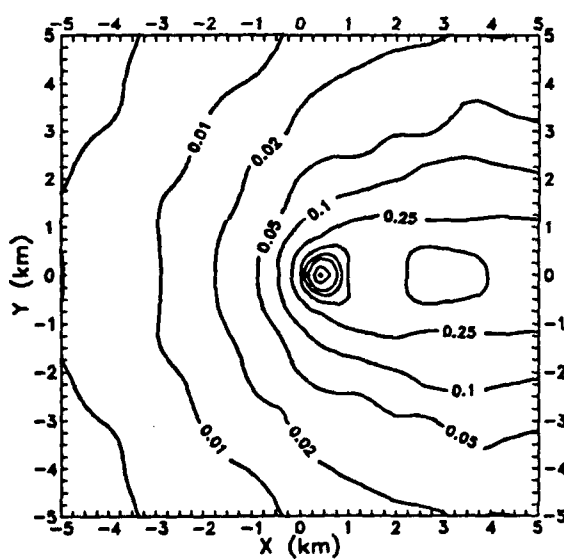
Note that there is a distinct decrease in the transient peak in the direction $(\theta, \phi) = (75^\circ, 0^\circ)$. This corresponds to the angle at which the observer is directly in line with the end-fire direction of simulator segment (A-B) of Figure 3-9. Note also in Figure 4-8b that as the observer comes close to the ground, the response becomes small, since the surface wave is neglected in the analysis. However, as shown in Figure 4-4, the surface wave contribution just on the earth's surface is not very large compared with the fields at higher altitudes. Consequently, the absence of the surface wave in Figure 4-8 is not critical in illustrating the overall shape of the peak radiated fields.



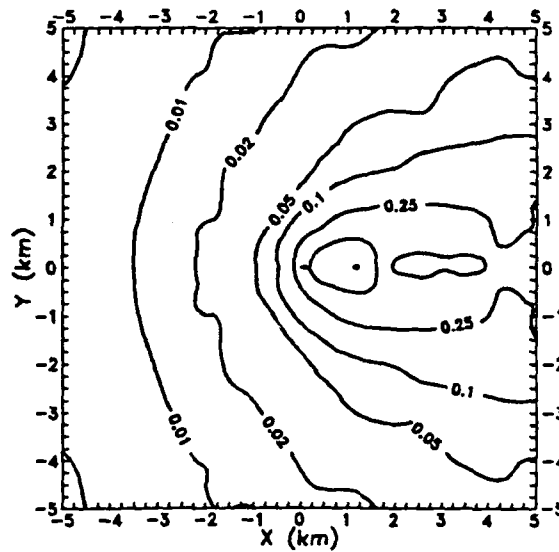
(a) $z = 50$ m



(b) $z = 100$ m

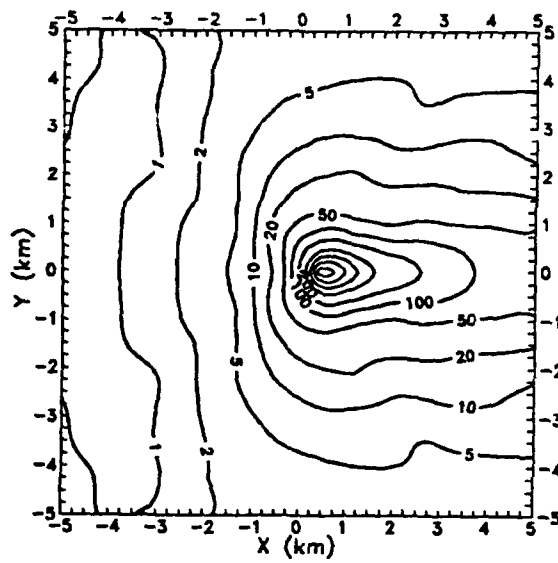


(c) $z = 250$ m

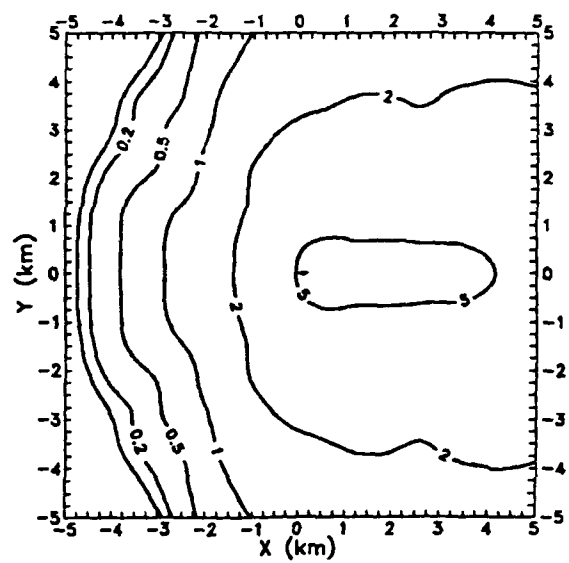


(d) $z = 500$ m

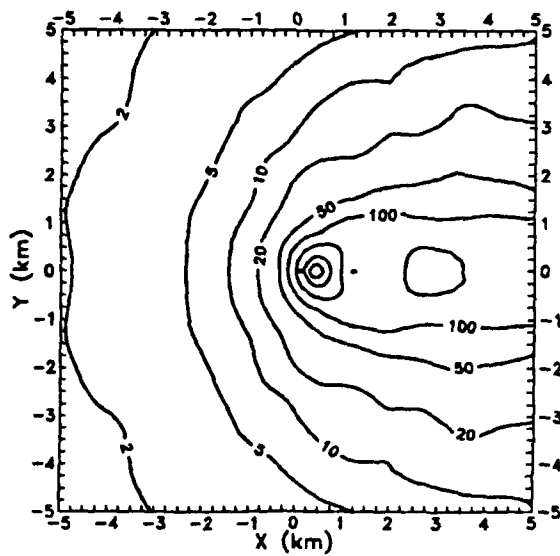
Figure 4-6. Contours of peak H-field (in A/m) for different altitudes.



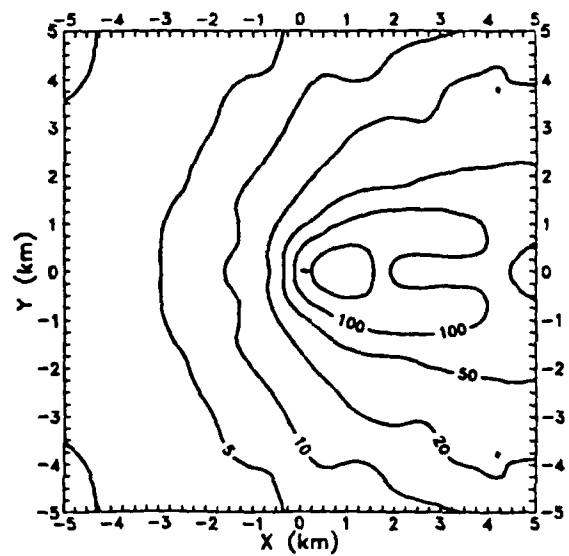
(a) $z = 50$ m



(b) $z = 100$ m

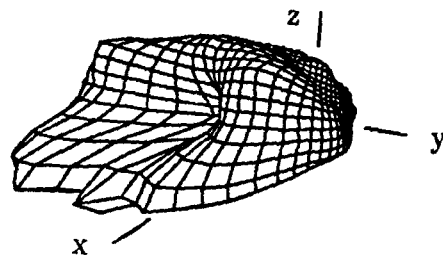


(c) $z = 250$ m

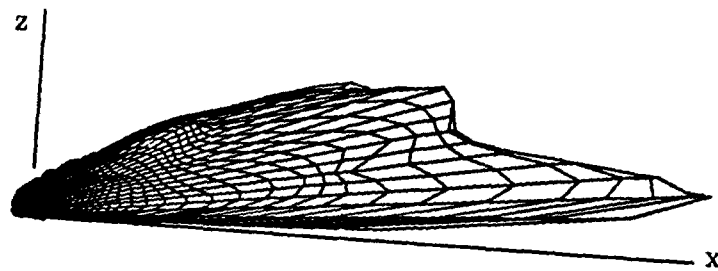


(d) $z = 500$ m

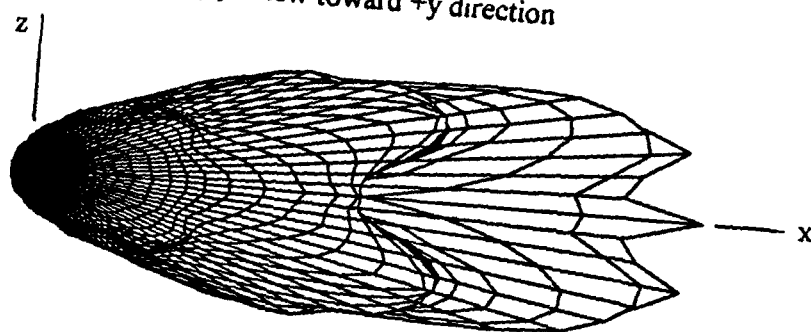
Figure 4-7. Contours of peak E-field (in V/m) for different altitudes.



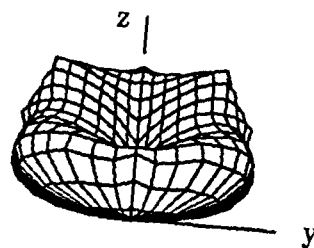
(a) Perspective view



(b) View toward $+y$ direction



(c) Top view toward $-z$ direction



(d) Front view toward $-x$ direction

Figure 4-8. Spatial peak of distant E and H-field patterns.

4.6 E AND H-FIELDS NEAR THE SIMULATOR.

The ARES field model will also permit the calculation of the E- and H-fields closer to the simulator. If the observer is too close to ARES, however, the assumption that the simulator plate current can be approximated by a current filament is invalid, and the calculated fields will be in error. Rough estimates of this suggest that the observer should be at least several plate widths away from the simulator structure for the model to be accurate. This suggests that the observation distance should be at least 100 m or more.

Keeping this limitation in mind, Figure 4-9 presents contours of the spatial variations of the H-field peaks in a 500×500 m region surrounding ARES. Figure 4-10 presents the behavior of the local E-field. Clearly the peak E-field is approaching the 30-50 kV/m levels in the working volume. In these plots, the outline of ARES is shown.

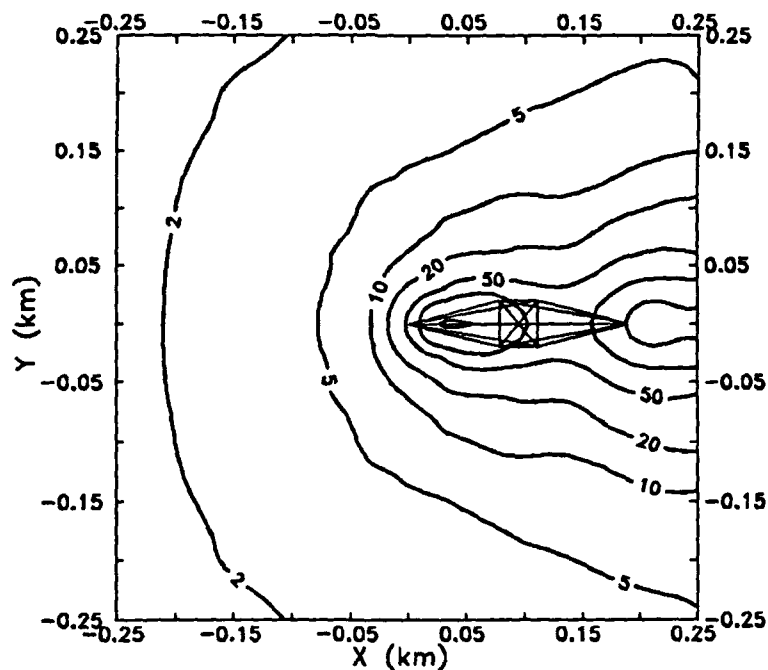


Figure 4-9. Contours of peak H-field (A/m) on the ground near the simulator.

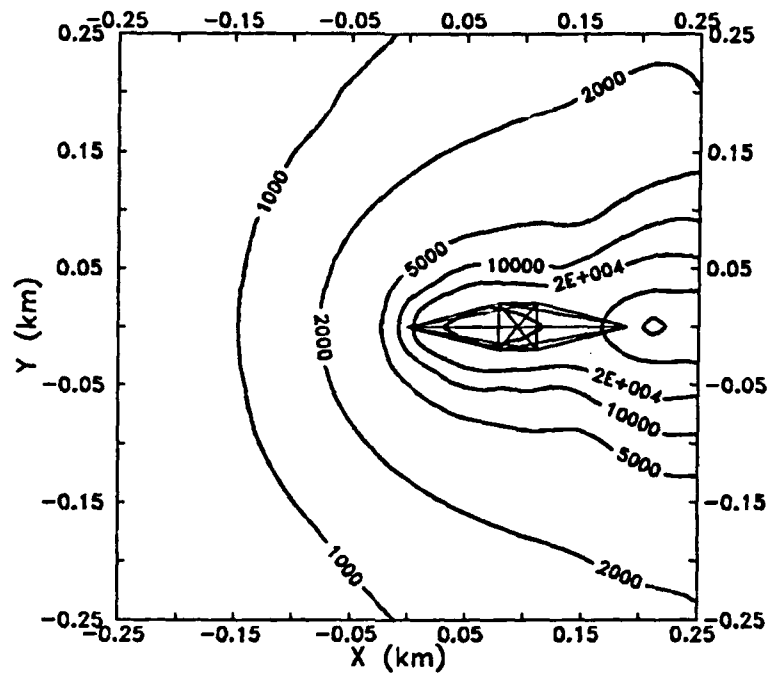


Figure 4-10. Contours of peak E-Field (V/m) on the ground near the simulator.

SECTION 5

ESTIMATES OF TERRAIN EFFECTS

The radiation of ARES fields is affected somewhat by variations in the local terrain. The simulator is located at the bottom of a deep trough, and as seen in the measurements in Figure 3-4, there is an asymmetry in the measured fields in the north-south direction. The high frequency field components radiated from the simulator can be diffracted by the bluff surrounding the simulator, and the low frequency components are affected by an additional propagation loss due to the longer path that the surface wave must take to pass over the irregular terrain.

Unfortunately, there is no analytical solution available to this problem. However, an examination of the measured data indicates that this effect is not severe and the present flat-earth model gives results that compare very well with measured data. However, to investigate this terrain effect further, a low-frequency path-length correction model was developed to account for the irregular terrain.

The ARES facility is located just off of a flat mesa area, as shown in the topographical map in Figure 5-1. To the north of the simulator lies a bluff which is about 50 feet high, and to the south is a gently sloping region. The ground contours in the vicinity of ARES were digitized and used in a calculation of the variations of the surface wave path from the simulator working volume to a distant ground observation point. Figure 5-2a shows the ground contours in the vicinity of ARES, with the simulator outline indicated. Figure 5-2b shows a surface plot of the same region.

For a wave from the simulator midpoint to a distant observation point, it travels along a path as indicated by the straight line shown in Figure 5-2. For this particular path, Figure 5-3 shows the ground elevation as a function of the horizontal distance. The line integral along this cut gives the actual path length over which the wave must travel, and the difference between this value and the horizontal distance is the additional path length of the wave.

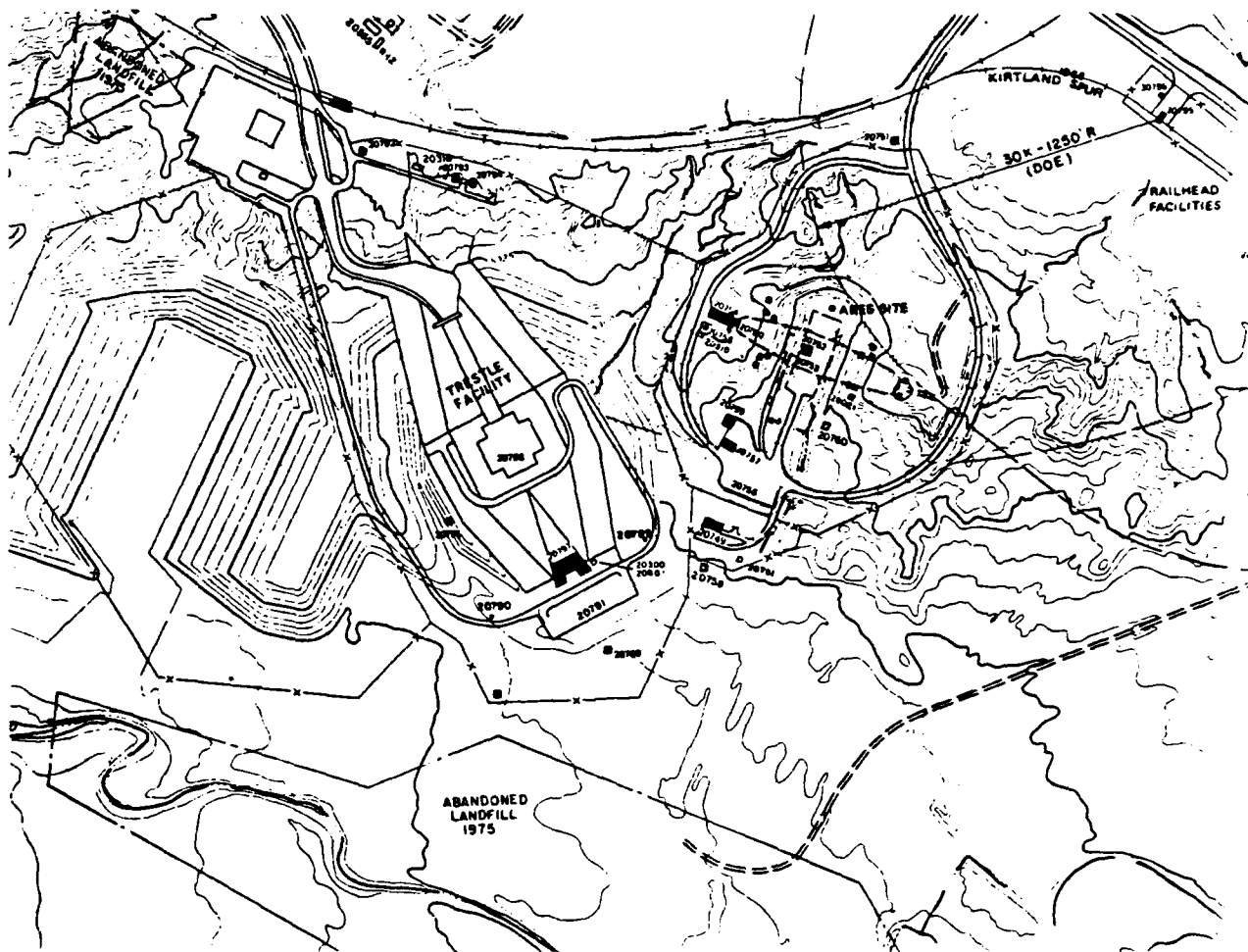
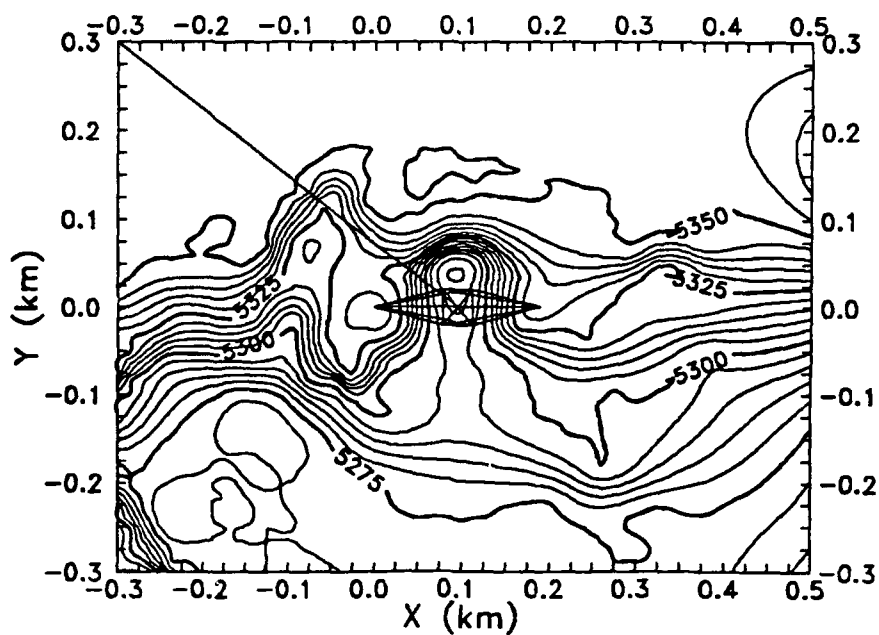
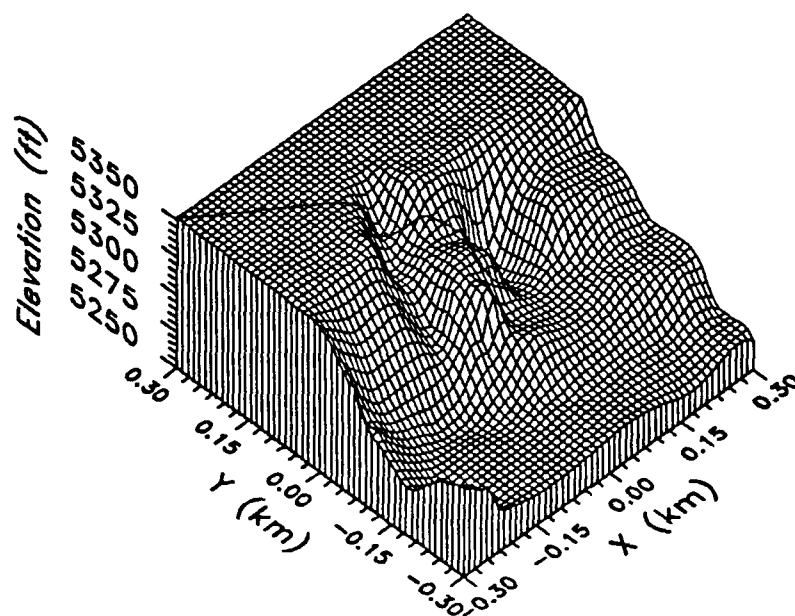


Figure 5-1. Ground topography near ARES.



(a) Contour plot (contours at 5 ft. intervals)



(b) Surface plot

Figure 5-2. Digitized ground topography.

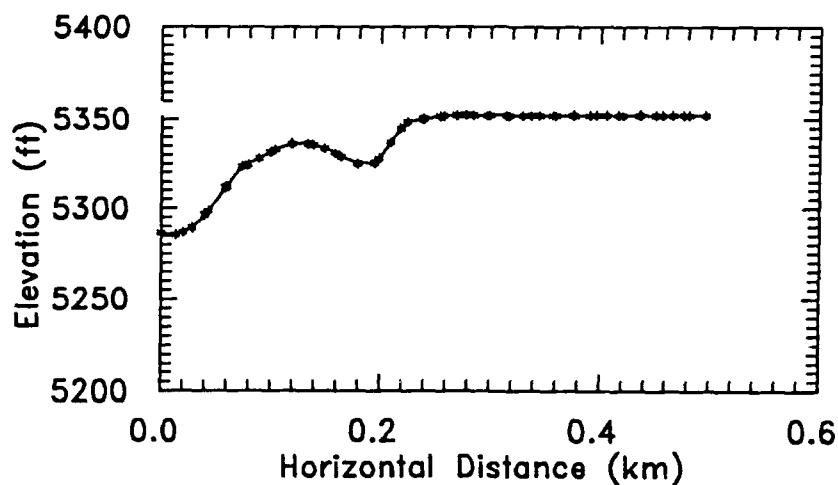


Figure 5-3. Ground elevation along the straight-line path in Figure 5-2.

Figure 5-4 shows the additional path length for an arbitrary ray path extending from the simulator center to a very distant point defined by the cylindrical angle ϕ measured with respect to the x-axis. The maximum additional path length is seen to be on the order of only 5 meters, and for many observation points which may not be very far away from the simulator, the path difference is much less. Calculations of the surface wave response using these different path lengths were performed, and some very small changes in the radiated fields were noted. However, when the E and H field contours were plotted, they were virtual overlays of Figures 3-4, and 3-5. This calculation substantiates the observation that the approximate additional path-length terrain effects are of secondary importance in determining the ground fields at large distances from the simulator. The accuracy of this approximation has not been studied in detail, however.

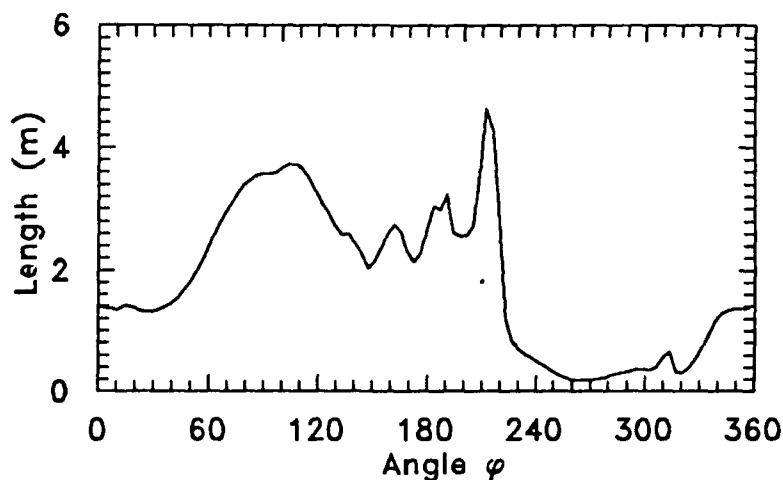


Figure 5-4. Additional surface wave path-length.

SECTION 6

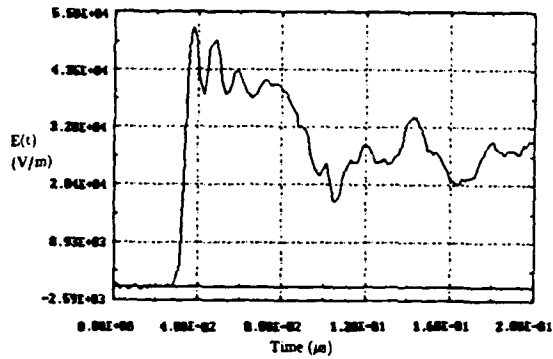
ARES PULSER RISE TIME EFFECTS

The ARES pulser has a rise time that can vary from about 2 to 10 ns. Using this calculational model, it is possible to study the effect of this rise time on the radiated field. A common misconception is that the radiated fields from such a simulator will be larger for a faster-rising pulser waveform. This notion comes from the fact that the radiated field from an infinitesimal current element $Id\xi$ is proportional to the time derivative of the current. This suggests that the faster the current changes, the larger the radiated field will be.

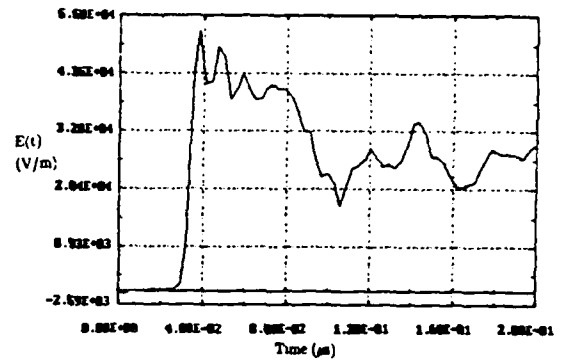
This fact is not true, however, for an extended current source. For the simple line current source shown in Figure 2-10, Equation 2.15 gives the radiated E-field which has an early-time response proportional to the current. Because the ARES fields are produced by a spatially extensive set of currents, it is expected that the radiated fields will not be strongly dependent on the pulser rise-time.

To study the effect of different pulser rise-times, it is possible to consider pulser waveforms having a different number of time sample points. This changes the effective rise time of the digitized excitation waveform used in the calculations. Figure 6-1 plots of the first 0.2 μ s of the ARES pulser waveform of Figure 2-2a. These plots are shown for $N = 128, 256, 512, 1024,$ and 2048 points for the entire transient waveform. The rise time of the excitation is well-defined for the larger number of sample points, but it becomes increasingly ill-defined and slower for fewer numbers of points.

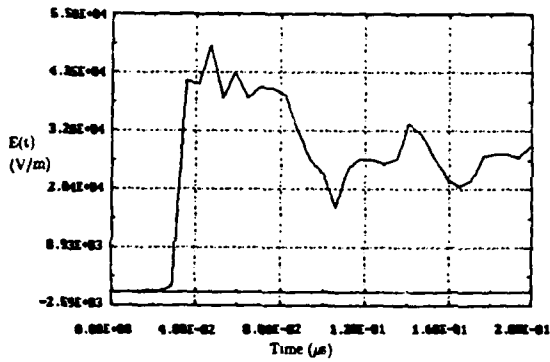
As an example of the radiated fields from ARES for these different excitations, Figure 6-2 shows the E_z -field in the air at location $(x,y,z) = (0.1, 20, 10)$ km. The overall radiated waveshape is remarkably stable as N varies. Of course, there is loss of internal structure of the waveform, but its peak amplitude remains robust. Figure 6-3 illustrates the similar behavior of the E_z -field component on the ground at $(x,y,z) = (0.1, 2, 0)$ km. For this case, the $N = 2048$ point case was not computed due to the large amount of computer time required. For these latter ground location calculations, the fine detail in the waveforms is missing, due to the high-frequency attenuation of the surface wave. These plots confirm the fact that the radiated fields are relatively insensitive to the pulser rise-time.



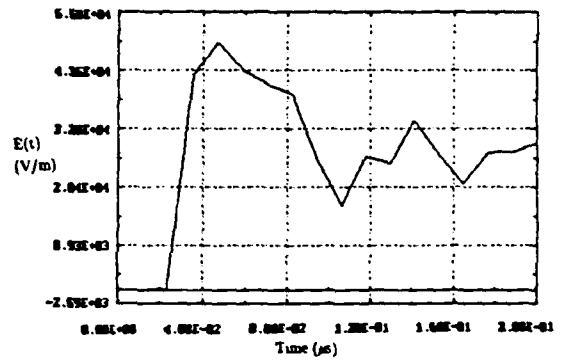
(a) $N = 2048$



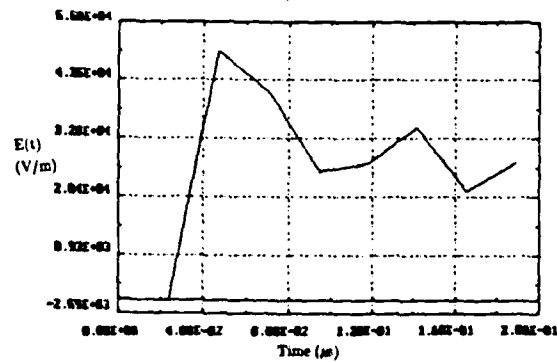
(b) $N = 1024$



(c) $N = 512$

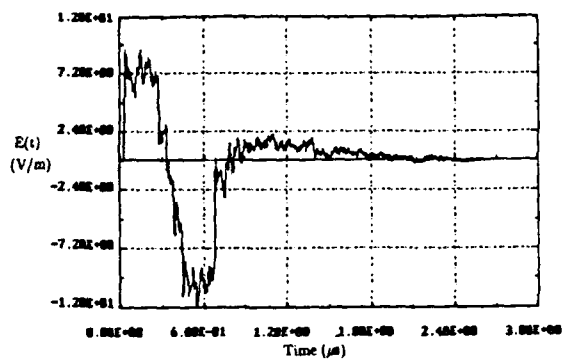


(d) $N = 256$

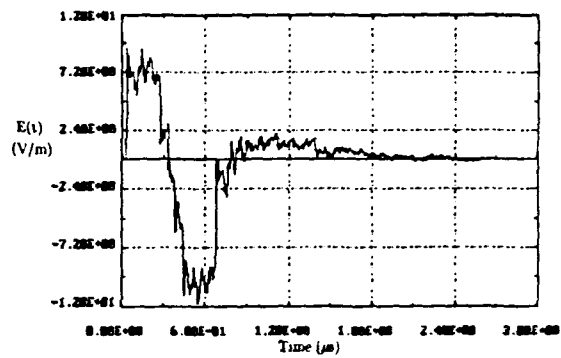


(e) $N = 128$

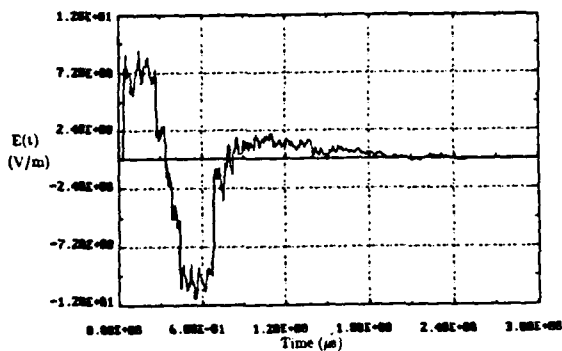
Figure 6-1. ARES excitation waveform for various N .



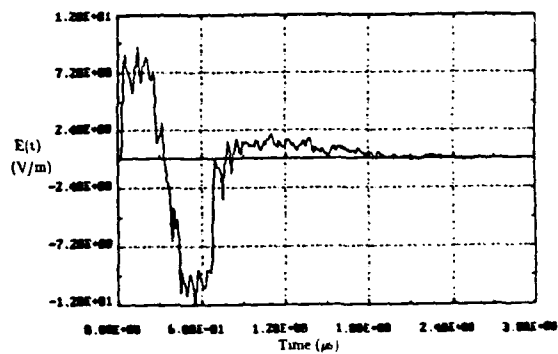
(a) $N = 2048$



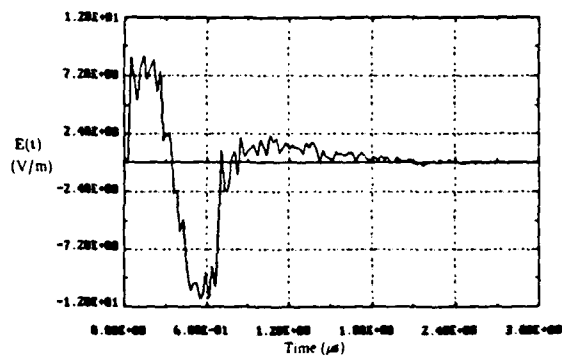
(b) $N = 1024$



(c) $N = 512$



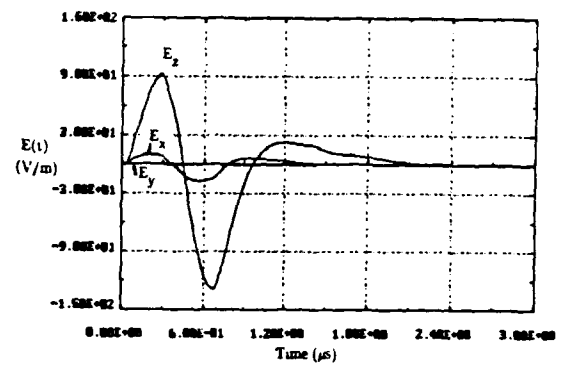
(d) $N = 256$



(e) $N = 128$

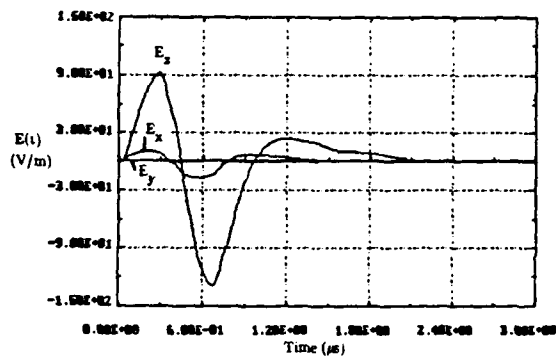
Figure 6-2. E_z -field in the air at $(x,y,z) = (0.1, 20, 10)$ km for various N .

Not Calculated

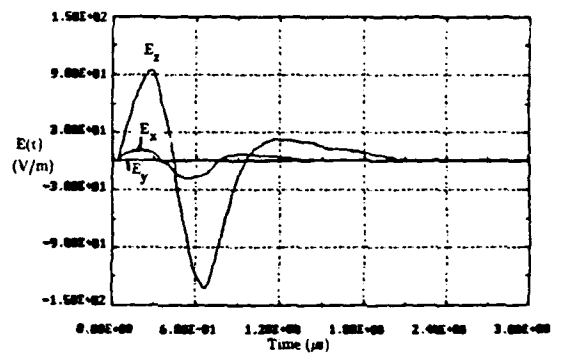


(a) $N = 2048$

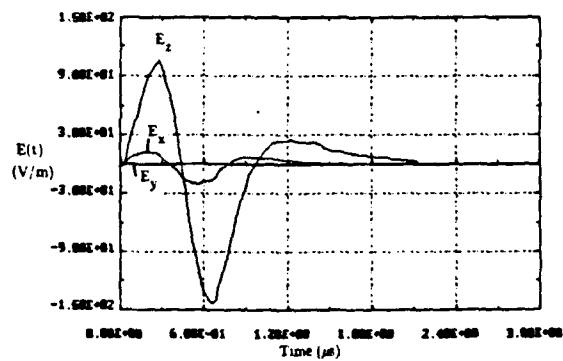
(b) $N = 1024$



(c) $N = 512$



(d) $N = 256$



(e) $N = 128$

Figure 6-3. E_z -field on the ground at $(x,y,z) = (0.1, 2, 0)$ km for various N .

SECTION 7

COMPUTER CODE DESCRIPTION

7.1 CODE OVERVIEW.

The analysis model described in this report has been implemented in a computer code. The code was used to compute all of the curves in the preceding sections. This program was written in standard FORTRAN and is designed to be run on PC-class computers. However, the code is transportable to VAX or Cray machines.

The overall calculational procedure for determining the radiated fields is presented in more detail in Figure 7-1. The measured ARES working volume E-field is used as an input to deduce an effective voltage waveform for the pulser, and the frequency-domain spectrum of this excitation is found by a FFT calculation. At each spectral frequency, the current flowing on the ARES simulator is determined using the transmission line model.

The spectra of the radiated E and H-fields produced by these currents are calculated at a distant observation point. This is done by integrating over the ARES current distribution. In most cases, a numerical integration is required. In this procedure, the effects of the lossy ground-plane are taken into account by the Fresnel reflection coefficients and the Norton surface wave. For distant, airborne observers, the required integrations may be performed analytically.

The radiated transient fields are constructed by a Fourier transform inversion of the spectra of the computed fields. This involves computing the field spectra at a number of different frequency points, typically 2^m points for the FFT, and then performing a numerical transform.

The computer program developed for this analysis reads the observation location (x,y,z) and the earth parameters, ϵ_g and σ_g , from a diskfile as input data. It also reads a control flag to delete the surface or sky wave contributions to the solution if desired, and a flag to perform the alternate (fast) integration of the radiated fields that neglects the surface wave contributions. The ARES excitation waveform, or any other desired waveform, is also read from a diskfile. The output data from this code are the transient E -and H-field components which are written to disk files.

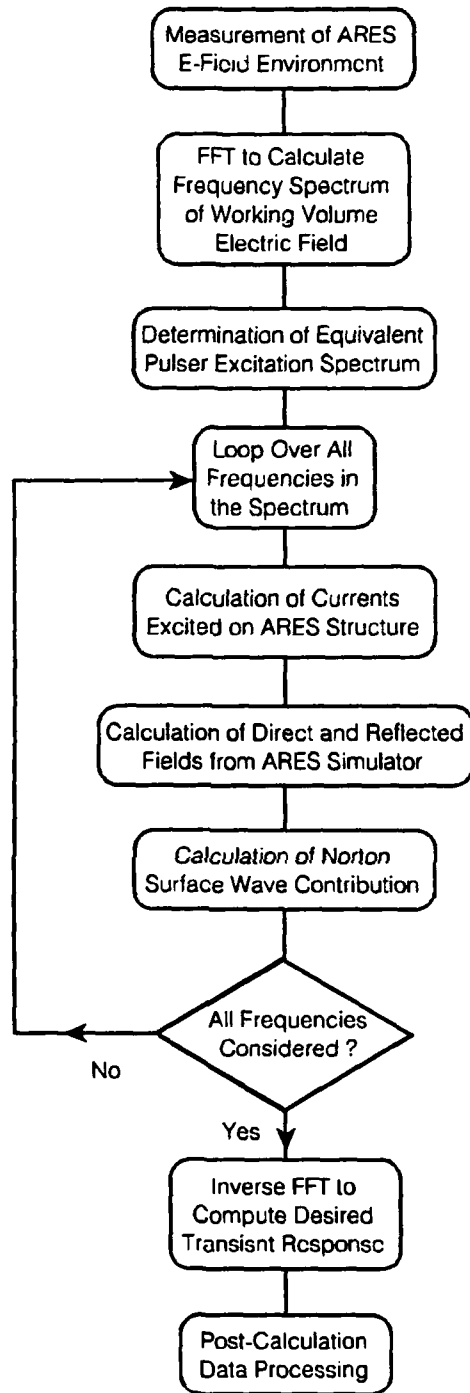


Figure 7-1. Summary of the ARES calculational procedure.

For the PC machines, there is an additional driving program that provides a user interface to the FORTRAN code. This interface will automatically generate the ARES driving waveform with the proper 2^m sample points and has an option for storing just the peak values of the calculated fields. This is beneficial if many calculations are to be performed and disk storage of the entire transient records is not feasible. This driver has an easy user-interface with pull-down menus and an integrated screen plot/graphics routine for obtaining hard copy of plots. This, however, operates only on the PC and cannot be transported to other machines.

7.2 COMPUTER REQUIREMENTS FOR ANALYSIS.

The actual analysis is straightforward, but time consuming, due to the numerical integration and evaluation of the surface wave. The required computer time for conducting an analysis of the fields depends both on the type of computer used, and on the requirements of the analysis. The FFT algorithm limits the number of time domain response points to 2^m , as 512, 1024, etc. A smaller number of points in the waveform means a faster calculation but provides an increasingly poor resolution of the response in time.

For a 33 MHz 80386/80387 PC, Figure 7-2 summarizes typical computer time requirements. This figure gives the CPU time for calculating the transient response at one observation point for different numbers of points in the waveform. The computed response actually consists of six separate transient waveforms, as all three vector components of both E and H are computed.

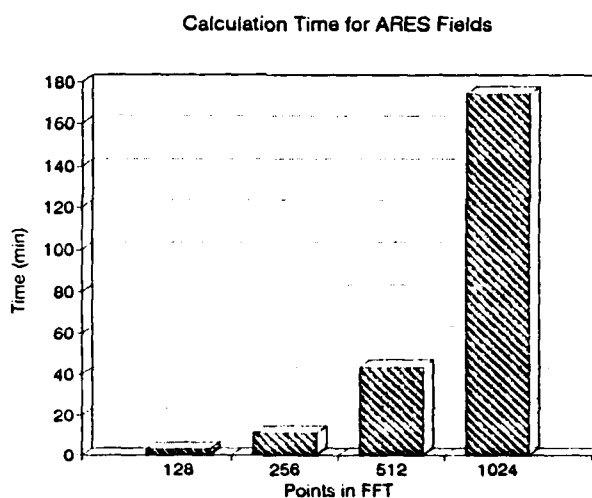


Figure 7-2. Computer time requirements for analysis.

SECTION 8

SUMMARY

A simple analysis procedure has been developed for approximately computing the radiated fields on the ground or in the air from ARES. This model employs transmission line theory to determine the simulator current distribution. Once this current is determined, the radiated fields are computed by integrating over the currents using a Green's function containing the Norton surface-wave contributions.

A comparison of the calculated responses with the limited measured H-field data provides a way of validating the accuracy of this analysis. This check of these data showed very good agreement between the two. This agreement is surprisingly good, considering the approximate nature of the modeling. In addition, checks on the physical reasonableness of the calculated responses have been made to insure that the analysis and computer code are operating correctly.

The numerical calculations of the model have determined that the far fields on the ground are due primarily to the Norton surface wave contribution. These fields have a slow rise time and tend to decay faster than $1/r$ with the distance from the simulator. The fields in the air have a faster rise than on the ground, and can be significantly larger in amplitude. For observation heights over 100 to 200 meters, the surface wave contribution to the radiated fields has been shown to be relatively small and may be neglected.

A very crude estimate for modifying the fields on the ground due to variations of the local terrain provided only a very small correction to the responses. Furthermore, the experimental results showed also only a small effect. In a practical and general sense, the terrain effects seem to be unimportant. However, there could be important implications in some particular region of the angle-frequency parameter space. This remains to be determined.

The effect of changing the rise time of the ARES pulser has been investigated. It is found that the pulser rise-time is not a critical factor in determining the radiated fields away from the simulator.

REFERENCES

1. ARES Facility User's Manual, Field Command, Defense Nuclear Agency, Kirtland Air Force Base, February 22, 1991.
2. Baum, C.E., "EMP Simulators for Various Types of Nuclear EMP Environments: An Interim Categorization," *IEEE Trans. EMC*, Vol. EMC-20, No.1, Feb. 1978.
3. Baum, Lt. C.E., *Impedances and Field Distributions for Parallel Plate Transmission Line Simulators*, Sensor and Simulation Notes, Air Force Weapons Laboratory, Kirtland AFB, New Mexico, June 6, 1966.
4. Baum, C.E., D.V. Giri, and R.D. Gonzalez, *Electromagnetic Field Distribution of the TEM Mode in a Symmetrical Two-Parallel-Plate Transmission Line*, Sensor and Simulation Note 219, Air Force Weapons Laboratory, Kirtland AFB, New Mexico, April 1, 1976.
5. Brown, T.L., and K.D. Granzow, *A Parameter Study of Two Parallel Plate Transmission Line Simulators*, Sensor and Simulation Note 21, Air Force Weapons Laboratory, Kirtland AFB, New Mexico, April 19, 1968.
6. Hutchins, R.L., *ARES Facility Description Electromagnetic Environment Vol. II*, ARES Memo 5, Air Force Weapons Laboratory, Kirtland AFB, New Mexico, March 12, 1974.
7. Baum, C.E., and D.V. Giri, *Low Frequency Distant Fields for ATLAS I and II and Comparison with ALECS and ARES*, ATLAS Memo 19, Air Force Weapons Laboratory, Kirtland AFB, New Mexico, October 29, 1976.
8. Estes, J.C., et.al., *Test Report for the ARES Field Environment Mapping*, DNA-TR-90-182, BDM International, Albuquerque, NM., September 1991.
9. Tai, C.T., *Dyadic Green's Functions in Electromagnetic Theory*, Intext Educational Publishers, Scranton, PA. 1971.
10. Van Bladel, J., *Electromagnetic Fields*, McGraw Hill, New York, 1964.
11. Bingham, E.O., *The Fast Fourier Transform*, Prentice Hall, Englewood Cliffs, NJ, 1974.
12. King, R.W.P., *Transmission Line Theory*, Dover Publications, 1965.
13. Tesche, F.M., "An Overview of Transmission Line Analysis," *Proceedings of the International Conference on Electromagnetic Compatibility*, EMC Expo 1987, San Diego, CA, May 19-21, 1987.
14. Jordan, E.C., and K.G. Balmain, *Electromagnetic Waves and Radiating Systems*, Prentice-Hall, 1968.

15. Norton, K.A., "The Propagation of Radio Waves Over the Surface of the Earth And In The Upper Atmosphere", *Proc. IRE*, 24, 1936, and IRE, 25, 1937.
16. Sommerfeld, A., *Partial Differential Equations in Physics*, Academic Press, New York, 1964.
17. Vance, E.F., *Coupling to Shielded Cables*, Krieger Pub., 1987.
18. Plonsey, R., and R.E. Collin, *Principles and Applications of Electromagnetic Fields*, McGraw-Hill, New York, 1961.
19. Private communication with William Shoup, DNA Field Command, Albuquerque, NM, January 1992.

APPENDIX ACRONYMS

A	amperes
A/m	amperes per meter
ac	alternating current
ARES	Advanced Research EMP Simulator
B-dot	magnetic field time derivative
CPU	central processor unit
dc	direct current
DNA	Defense Nuclear Agency
E-field	electric fields
EM	electromagnetic
EMP	electromagnetic pulse
FFT	fast Fourier transform
H-field	magnetic field
km	kilometers
kV	kilovolts
kV/m	kilovolts per meter
m	meters
MHz	megahertz
μ s	microseconds
ns	nanoseconds
PC	personal computer
S/m	Siemens per meter
TEM	transverse electromagnetic
V	volts
V/m	volts per meter
VPD	vertically polarized dipole

DISTRIBUTION LIST

DNA-TR-92-153

DEPARTMENT OF DEFENSE

ARMED FORCES RADIOBIOLOGY RSCH INST
ATTN: DR M R LANDAUER

ASSISTANT TO THE SECRETARY OF DEFENSE
ATTN: EXECUTIVE ASSISTANT

DEFENSE INFORMATION SYSTEMS AGENCY
ATTN: COMMANDER

DEFENSE INTELLIGENCE AGENCY
ATTN: DIW-4
ATTN: DT-5A R BURGER
ATTN: VP-TPO

DEFENSE NUCLEAR AGENCY
ATTN: RAAE K SCHWARTZ
2 CY ATTN: RAAE
2 CY ATTN: TITL

DEFENSE TECHNICAL INFORMATION CENTER
2 CY ATTN: DTIC/OC

FIELD COMMAND DEFENSE NUCLEAR AGENCY
2 CY ATTN: FCTT W SHOUP
2 CY ATTN: NMOP LT COL R GWYN

NATIONAL DEFENSE UNIVERSITY
ATTN: NWCO

NET ASSESSMENT
ATTN: DOCUMENT CONTROL

STRATEGIC & SPACE SYSTEMS
ATTN: DR E SEVIN

DEPARTMENT OF THE ARMY

ARMY RESEARCH LABORATORIES
ATTN: TECH LIB
ATTN: SLCHD-NW
ATTN: SLCHD-NW-CS LOU JASPER JR
ATTN: SLCHD-NW-E E L PATRICK
2 CY ATTN: SLCHD-NW-E R L ATKINSON
ATTN: SLCHD-NW-EP
ATTN: SLCHD-NW-RP
ATTN: SLCHD-NW-TN
ATTN: SLCHD-NW-TN G MERKEL
ATTN: W PATTERSON

DEPT CH OF STAFF FOR OPS & PLANS
ATTN: DAMO-ODW

NUCLEAR EFFECTS DIVISION
ATTN: STEWS-NE J MEASON

PEO COMMUNICATION
ATTN: J BOWDEN
ATTN: V PHILLIPUK

U S ARMY ATMOSPHERIC SCIENCES LAB
ATTN: SLCAS-AS

U S ARMY BALLISTIC RESEARCH LAB
ATTN: SLCBR-SS-T
ATTN: SLCBR-TB-B G BULMASH
ATTN: SLCBR-VL

U S ARMY ENGINEER DIV HUNTSVILLE
ATTN: CEHND-SY J LOYD
ATTN: HNDED-SY

U S ARMY NUCLEAR & CHEMICAL AGENCY
ATTN: MONA-NU DR D BASH

U S ARMY SPACE & STRATEGIC DEFENSE CMD
ATTN: CSSD-SL

U S ARMY STRATEGIC SPACE & DEFENSE CMD
ATTN: CSSD-SA-E

U S ARMY TEST & EVALUATION COMMAND
ATTN: TECHNICAL LIBRARY SI-F

U S ARMY WAR COLLEGE
ATTN: LIBRARY

US ARMY MATERIEL SYS ANALYSIS ACTVY
ATTN: AMXSY-CR

USA SURVIVABILITY MANAGMENT OFFICE
ATTN: SLCSM-SE J BRAND

DEPARTMENT OF THE NAVY

NAVAL AIR SYSTEMS COMMAND
ATTN: AIR 5161

NAVAL AIR TEST CENTER
ATTN: SY84

NAVAL CIVIL ENGINEERING LABORATORY
ATTN: L72 JAMES BROOKS

NAVAL POSTGRADUATE SCHOOL
ATTN: CODE 1424 LIBRARY
ATTN: X MARUYAMA
ATTN: PROF DONALD L WALTERS

NAVAL RESEARCH LABORATORY
ATTN: CODE 5227 RESEARCH REPORT

NAVAL SURFACE WARFARE CENTER
ATTN: CODE H25 G BRACKETT
ATTN: CODE R41
ATTN: CODE 425

NAVAL SURFACE WARFARE CENTER
ATTN: CODE H-21

OFFICE OF CHIEF OF NAVAL OPERATIONS
ATTN: NOP 098
ATTN: NOP 551
ATTN: NOP 941F
ATTN: N88OE
ATTN: OP 654

THEATER NUCLEAR WARFARE PROGRAM OFC
ATTN: PMS 423 CDR DOOLING

DNA-TR-92-153 (DL CONTINUED)

DEPARTMENT OF THE AIR FORCE

AIR FORCE CTR FOR STUDIES & ANALYSIS
ATTN: AFSAA/SAKI

AIR FORCE SPACE COMMAND
ATTN: DEES/D C DE MIO

AIR UNIVERSITY LIBRARY
ATTN: AUL-LSE

OKLAHOMA CITY AIR LOGISTICS CTR/TIES
ATTN: TIESW 1LT A POPOVICH

SPACE DIVISION/IN
ATTN: IND

DEPARTMENT OF ENERGY

LAWRENCE LIVERMORE NATIONAL LAB
ATTN: L-86 H CABAYAN

LOS ALAMOS NATIONAL LABORATORY
ATTN: REPORT LIBRARY

OAK RIDGE NATIONAL LABORATORY
ATTN: R BARNES

SANDIA NATIONAL LABORATORIES
ATTN: ORG 9300 J E POWELL
ATTN: TECH LIB 3141

U S DEPT OF ENERGY IE-24
ATTN: J BUSSE

DEPARTMENT OF DEFENSE CONTRACTORS

ALLIED-SIGNAL, INC
ATTN: DOCUMENT CONTROL

BDM FEDERAL INC
ATTN: E DORCHAK

BDM FEDERAL INC
ATTN: B TORRES
ATTN: L O HOEFT
ATTN: B PLUMMER

BOEING CO
ATTN: D EGELKROUT
ATTN: D CHAPMAN

BOEING TECHNICAL & MANAGEMENT SVCS, INC
ATTN: ARNOLD D BAKER

BOOZ ALLEN & HAMILTON INC
ATTN: D VINCENT
ATTN: T J ZWOLINSKI

BOOZ-ALLEN & HAMILTON, INC
ATTN: TECHNICAL LIBRARY

COMPUTER SCIENCES CORP
ATTN: A SCHIFF

E-SYSTEMS, INC
ATTN: TECH INFO CTR

EG&G SPECIAL PROJECTS INC
ATTN: J GILES

ELECTRO-MAGNETIC APPLICATIONS, INC
ATTN: TECH LIBRARY

FAIRCHILD SPACE COMPANY
ATTN: R CARPENTER

HONEYWELL SYSTEMS & RESEARCH CENTER
ATTN: T CLARKIN

INSTITUTE FOR DEFENSE ANALYSES
ATTN: CLASSIFIED LIBRARY
ATTN: TECH INFO SERVICES

JAYCOR
ATTN: J WONDRA

JAYCOR
ATTN: C KNOWLES
ATTN: E WENAAS
ATTN: M SCHULTZ JR

KAMAN SCIENCES CORP
ATTN: DASIAC
ATTN: E CONRAD

KAMAN SCIENCES CORPORATION
ATTN: DASIAC
ATTN: R RUTHERFORD

KEARFOTT GUIDANCE AND NAVIGATION CORP
ATTN: J D BRINKMAN

LITTON SYSTEMS, INC
ATTN: J SKAGGS

LOCKHEED MISSILES & SPACE CO, INC
ATTN: G LUM
ATTN: TECH INFO CTR

LOCKHEED SANDERS, INC
ATTN: BRIAN G CARRIGG

LOGICON R & D ASSOCIATES
2 CY ATTN: C MO
ATTN: DOCUMENT CONTROL
2 CY ATTN: F TESCHE
ATTN: G K SCHLEGEL

LOGICON R & D ASSOCIATES
ATTN: E QUINN

LOGICON R & D ASSOCIATES
ATTN: J P CASTILLO
ATTN: W S KEHRER

LTV AEROSPACE & DEFENSE COMPANY
2 CY ATTN: LIBRARY EM-08

METATECH CORP
ATTN: C JONES

MISSION RESEARCH CORP
ATTN: EMP GROUP
ATTN: J CARRON
ATTN: TECH INFO CENTER

MISSION RESEARCH CORP
ATTN: A CHODOROW

MISSION RESEARCH CORP
ATTN: J LUBELL
ATTN: J R CURRY

MITRE CORPORATION
ATTN: M FITZGERALD

MITRE CORPORATION
ATTN: DIRECTOR

PACIFIC-SIERRA RESEARCH CORP
ATTN: H BRODE

PHOTOMETRICS, INC
ATTN: I L KOFSKY

PHYSITRON INC
ATTN: MARION ROSE

RAND CORP
ATTN: ENGR & APPLIED SCIENCES DEPT

RESEARCH TRIANGLE INSTITUTE
ATTN: M SIMONS

ROCKWELL INTERNATIONAL CORP
ATTN: J C ERB

ROCKWELL INTERNATIONAL CORP
ATTN: P BELL

S-CUBED
ATTN: J KNIGHTEN
ATTN: LLOYD DUNCAN

SCIENCE & ENGRG ASSOCIATES, INC
ATTN: R M SMITH

SCIENCE APPLICATIONS INTL CORP
ATTN: J RETZLER

SCIENCE APPLICATIONS INTL CORP
ATTN: W ADAMS
ATTN: W CHADSEY
ATTN: W LAYSON

SRI INTERNATIONAL
ATTN: E VANCE
ATTN: W GRAF

TELEDYNE BROWN ENGINEERING
ATTN: LEWIS T SMITH
ATTN: RONALD E LEWIS

TRW
ATTN: M J TAYLOR

TRW INC
ATTN: LIBPARIAN

UNISYS CORPORATION-DEFENSE SYSTEMS
ATTN: TECHNICAL LIBRARY

UNITED TECHNOLOGIES CORP
ATTN: R D TOTTON

FOREIGN

DEFENCE RESEARCH ESTABLISHMENT OTTAWA
ATTN: S KASHYAP